The Astrophysical Journal, 648:323–339, 2006 September 1


# A *SPITZER SPACE TELESCOPE*[1] INFRARED SPECTROGRAPH[2] SURVEY OF WARM MOLECULAR HYDROGEN IN ULTRALUMINOUS INFRARED GALAXIES

S. J. U. Higdon,[3] L. Armus,[4] J. L. Higdon,[3] B. T. Soifer,[4] and H. W. W. Spoon[3]
*Received 2006 March 10; accepted 2006 May 10*

## ABSTRACT

We have conducted a survey of ultraluminous infrared galaxies (ULIRGs) with the Infrared Spectrograph on the *Spitzer Space Telescope*, obtaining spectra from 5.0 to 38.5 $\mu$m for 77 sources with $0.02 < z < 0.93$. Observations of the pure rotational $H_2$ lines $S(3)$ 9.67 $\mu$m, $S(2)$ 12.28 $\mu$m, and $S(1)$ 17.04 $\mu$m are used to derive the temperature and mass of the warm molecular gas. We detect $H_2$ in 77% of the sample, and all ULIRGs with $F_{60\,\mu m} > 2$ Jy. The average warm molecular gas mass is $\sim 2 \times 10^8\ M_\odot$. High extinction, inferred from the 9.7 $\mu$m silicate absorption depth, is not observed along the line of sight to the molecular gas. The derived $H_2$ mass does not depend on $F_{25\,\mu m}/F_{60\,\mu m}$, which has been used to infer either starburst or AGN dominance. Similarly, the molecular mass does not scale with the 25 or 60 $\mu$m luminosities. In general, the $H_2$ emission is consistent with an origin in photodissociation regions associated with star formation. We detect the $S(0)$ 28.22 $\mu$m emission line in a few ULIRGs. Including this line in the model fits tends to lower the temperature by $\sim$50–100 K, resulting in a significant increase in the gas mass. The presence of a cooler component cannot be ruled out in the remainder of our sample, for which we do not detect the $S(0)$ line. The measured $S(7)$ 5.51 $\mu$m line fluxes in six ULIRGs implies $\sim 3 \times 10^6\ M_\odot$ of hot ($\sim$1400 K) $H_2$. The warm gas mass is typically less than 1% of the cold gas mass derived from $^{12}$CO observations.

*Subject headings:* galaxies: active — galaxies: starburst — infrared: galaxies

## 1. INTRODUCTION

Ultraluminous infrared galaxies (ULIRGs) are the most luminous objects in the local universe. These objects appear to be mergers of dusty, gas-rich disk galaxies (e.g., Sanders & Mirabel 1996; Moorwood 1996). A direct result of this dusty and large optical depth environment is that they radiate 90% or more of their total energy in the far-infrared, typically with $L_{8-1000\,\mu m} \geq 10^{12}\ L_\odot$. The bolometric luminosities and space densities of ULIRGs in the local universe (i.e., $z \leq 0.1$) are similar to those of QSOs (Soifer et al. 1987; Sanders & Mirabel 1996). It was proposed by Sanders et al. (1988) that most ULIRGs are powered by dust-enshrouded QSOs in the late phases of a merger. A classic example of this is Mrk 231, where the detection of broad ($\sim$10,000 km s$^{-1}$) hydrogen emission lines (Arakelian et al. 1971; Adams & Weedman 1972) and radio jets (Lonsdale et al. 2003) provides direct evidence for the central active galactic nucleus (AGN). The final state of a ULIRG may be a large elliptical galaxy with a central massive quiescent black hole (Kormendy & Sanders 1992). The ratio of the 25 to 60 $\mu$m flux densities, as measured with the *Infrared Astronomical Satellite* (*IRAS*; Neugebauer et al. 1984), has been used to classify ULIRGs. This ratio reflects the globally averaged dust temperature of the galaxy, which is typically 50–100 K. The ULIRGs are classified as either "warm" ($F_{25\,\mu m}/F_{60\,\mu m} \geq 0.2$) and possibly AGN dominated or "cold" ($F_{25\,\mu m}/F_{60\,\mu m} < 0.2$), with a possible dominant contribution to the overall luminosity from massive star formation. Although luminous mergers are rare in the local universe, it has been proposed that ULIRGs may make a significant contribution to the star formation density at $z \geq 1$ (e.g., Elbaz & Cesarsky 2003).

Molecular hydrogen is the primary component of the dense gas in galaxies and the most abundant molecule in the universe. Stars are not only formed from molecular clouds, but the $H_2$ acts as a coolant enabling the star formation to proceed. $H_2$ may also act as a coolant facilitating the accretion of material onto a central AGN. Prior to space-borne missions large quantities of molecular hydrogen in the central regions of ULIRGs had been inferred from detections of rotational transitions of $^{12}$CO (e.g., Sanders et al. [1991] and references for this sample in Table 4). A much smaller, hot ($\sim$2000 K) gas component can be observed directly in the near-infrared through rovibrational $H_2$ lines (e.g., Van der Werf et al. 1993).

In this paper, we have used observations with the *Spitzer Space Telescope* (Werner et al. 2004) to directly probe the warm ($\gtrsim$100 K) molecular hydrogen component through pure rotational transitions, where the upper levels are populated via UV pumping, formation of $H_2$ in excited states, or collisional excitation. Four heating mechanisms have been proposed for the gas: (1) grain photoelectric heating in photodissociation regions (PDRs), (2) shock heating from outflows, supernova remnants (SNRs), and large-scale streaming motions in spiral arms and bars, (3) X-ray heating of gas from AGNs, SNRs, and cooling flows, and (4) cosmic-ray heating. $H_2$ has two independent states: ortho-$H_2$, where the nuclear spins are parallel, and para-$H_2$, where the spins are antiparallel. The rotational states have even spatial symmetry in the para-$H_2$ and odd spatial symmetry in the ortho-$H_2$. An ortho-to-para ratio of 3 is found for gas of typical temperature $T \sim 300$ K. The proton exchange mechanism is a pathway to set up and maintain these LTE ratios. $H_2$ is highly symmetric and has no permanent dipole moment. All the rotational transitions within the electronic ground state are quadrupolar, with correspondingly low spontaneous Einstein $A$-coefficients. This makes the emission lines very weak and, until the advent of *Spitzer*, difficult to observe in all but the brightest galaxies. Valentijn et al. (1996) published

[1] Based on observations obtained with the *Spitzer Space Telescope*, which is operated by the Jet Propulsion Laboratory, California Institute of Technology, for the National Aeronautics and Space Administration.

[2] The IRS was a collaborative venture between Cornell University and Ball Aerospace Corporation funded by NASA through the Jet Propulsion Laboratory and the Ames Research Center.

[3] Astronomy Department, Cornell University, Ithaca, NY 14853.

[4] *Spitzer* Science Center, California Institute of Technology, 220-6, Pasadena, CA 91125.

TABLE 1
ULIRG Sample

| Object | $z$ | $D_L$[a] (Mpc) | $L_{IR}$[b] ($10^{12}\ L_\odot$) | $F_{25\ \mu m}/F_{60\ \mu m}$ |
|---|---|---|---|---|
| 3C 273 | 0.1584 | 749.3 | 5.74 | 0.52 |
| Arp 220 | 0.0181 | 77.6 | 1.45 | 0.08 |
| IRAS 00188−0856 | 0.1286 | 596.3 | 2.56 | 0.14 |
| IRAS 00275−0044 | 0.2420 | 1203.8 | 2.62 | 0.37 |
| IRAS 00275−2859 | 0.2792 | 1418.1 | 3.16 | 0.25 |
| IRAS 00397−1312 | 0.2617 | 1316.5 | 6.46 | 0.22 |
| IRAS 00406−3127 | 0.3424 | 1797.9 | 6.25 | 0.12 |
| IRAS 00476−0054 | 0.7270 | 4462.9 | 8.32 | 0.11 |
| IRAS 01003−2238 | 0.1177 | 541.9 | 1.95 | 0.29 |
| IRAS 01199−2307 | 0.1560 | 736.6 | 2.32 | 0.10 |
| IRAS 02115+0226 | 0.4000 | 2160.1 | 9.65 | 0.49 |
| IRAS 02433+0110 | 0.7980 | 5009.1 | 8.91 | 0.23 |
| IRAS 03521+0028 | 0.1522 | 716.7 | 3.65 | 0.09 |
| IRAS 04114−5117 | 0.1246 | 576.2 | 1.85 | 0.04 |
| IRAS 04313−1649 | 0.2680 | 1352.9 | 4.48 | 0.07 |
| IRAS 05189−2524 | 0.0426 | 185.7 | 1.43 | 0.25 |
| IRAS 06035−7102 | 0.0795 | 356.3 | 1.66 | 0.11 |
| IRAS 06206−6315 | 0.0924 | 418.2 | 1.69 | 0.07 |
| IRAS 06301−7934 | 0.1564 | 738.7 | 2.45 | 0.05 |
| IRAS 06361−6217 | 0.1596 | 755.3 | 1.49 | 0.10 |
| IRAS 07598+6508 | 0.1488 | 699.5 | 3.37 | 0.31 |
| IRAS 08311−2459 | 0.1004 | 457.0 | 3.31 | 0.22 |
| IRAS 08572+3915 | 0.0584 | 257.6 | 1.37 | 0.23 |
| IRAS 09022−3615 | 0.0596 | 263.6 | 1.91 | 0.10 |
| IRAS 09463+8141 | 0.1547 | 729.8 | 2.03 | 0.05 |
| IRAS 10091+4704 | 0.2460 | 1226.5 | 4.55 | 0.07 |
| IRAS 10398+3247 | 0.6330 | 3762.8 | 6.03 | 0.04 |
| IRAS 10565+2448 | 0.0431 | 188.2 | 1.09 | 0.09 |
| IRAS 11119+3257 | 0.1890 | 911.1 | 4.51 | 0.22 |
| IRAS 12018+1941 | 0.1686 | 802.7 | 3.18 | 0.21 |
| IRAS 12032+1707 | 0.2170 | 1063.8 | 3.92 | 0.17 |
| IRAS 12072−0444 | 0.1284 | 595.2 | 2.30 | 0.22 |
| IRAS 12112+0305 | 0.0727 | 324.2 | 2.12 | 0.06 |
| IRAS 12514+1027 | 0.3000 | 1541.0 | 5.53 | 0.27 |
| IRAS 13120−5453 | 0.0308 | 133.0 | 1.73 | 0.07 |
| IRAS 13218+0552 | 0.2051 | 998.4 | 5.14 | 0.34 |
| IRAS 13342+3932 | 0.1793 | 859.2 | 1.96 | 0.02 |
| IRAS 13352+6402 | 0.2366 | 1173.3 | 3.64 | 0.08 |
| IRAS 13451+1232 | 0.1220 | 563.3 | 1.97 | 0.35 |
| IRAS 14348−1447 | 0.0825 | 370.6 | 2.24 | 0.07 |
| IRAS 14378−3651 | 0.0676 | 300.7 | 1.35 | 0.08 |
| IRAS 14537+1950 | 0.6400 | 3814.0 | 10.49 | 0.57 |
| IRAS 14548+3349 | 0.4430 | 2440.0 | 2.82 | 0.18 |
| IRAS 15001+1433 | 0.1627 | 771.7 | 2.79 | 0.09 |
| IRAS 15206+3342 | 0.1244 | 575.3 | 1.73 | 0.20 |
| IRAS 15250+3609 | 0.0554 | 244.0 | 1.13 | 0.18 |
| IRAS 15462−0450 | 0.0998 | 453.8 | 1.59 | 0.15 |
| IRAS 16124+3241 | 0.7100 | 4334.3 | 4.57 | 0.31 |
| IRAS 16334+4630 | 0.1910 | 921.9 | 2.89 | 0.08 |
| IRAS 17068+4027 | 0.1791 | 858.2 | 2.43 | 0.09 |
| IRAS 17179+5444 | 0.1475 | 692.5 | 1.98 | 0.15 |
| IRAS 17208−0014 | 0.0430 | 187.8 | 2.50 | 0.05 |
| IRAS 17233+3712 | 0.6890 | 4176.6 | 10.51 | 0.25 |
| IRAS 17463+5806 | 0.3090 | 1594.8 | 2.69 | 0.06 |
| IRAS 18030+0705 | 0.1458 | 683.8 | 1.90 | 0.30 |
| IRAS 18443+7433 | 0.1347 | 627.4 | 2.08 | 0.09 |
| IRAS 19254−7245 | 0.0617 | 273.1 | 1.21 | 0.23 |
| IRAS 19297−0406 | 0.0857 | 386.1 | 2.56 | 0.08 |
| IRAS 19458+0944 | 0.0999 | 454.6 | 2.32 | 0.07 |
| IRAS 20037−1547 | 0.1919 | 926.7 | 3.66 | 0.17 |
| IRAS 20087−0308 | 0.1057 | 482.5 | 2.80 | 0.05 |
| IRAS 20100−4156 | 0.1296 | 601.3 | 4.48 | 0.07 |
| IRAS 20414−1651 | 0.0871 | 392.5 | 1.70 | 0.08 |
| IRAS 20551−4250 | 0.0427 | 186.2 | 1.10 | 0.15 |
| IRAS 21272+2514 | 0.1508 | 709.6 | 1.40 | 0.36 |
| IRAS 22491−1808 | 0.0773 | 346.0 | 1.54 | 0.10 |
| IRAS 23128−5919 | 0.0446 | 194.9 | 1.07 | 0.15 |
| IRAS 23129+2548 | 0.1791 | 858.2 | 3.13 | 0.07 |
| IRAS 23365+3604 | 0.0645 | 286.0 | 1.47 | 0.11 |
| IRAS 23498+2423 | 0.2120 | 1036.3 | 2.99 | 0.20 |
| IRAS 23529−2119 | 0.4303 | 2356.5 | 4.68 | 0.48 |
| Mrk 231 | 0.0422 | 184.2 | 3.70 | 0.25 |
| Mrk 273 | 0.0378 | 164.3 | 1.42 | 0.10 |
| Mrk 463E | 0.0504 | 221.0 | 0.60 | 0.72 |
| Mrk 1014 | 0.1631 | 773.6 | 4.12 | 0.24 |
| NGC 6240 | 0.0245 | 105.4 | 0.69 | 0.15 |
| UGC 5101 | 0.0400 | 174.3 | 1.00 | 0.09 |

[a] The luminosity distance.
[b] The 8–1000 $\mu$m far-infrared luminosity, defined as $L_{IR} = 4\pi d_L^2 F_{IR}$ in units of $L_\odot$, with $F_{IR} = 1.8 \times 10^{-14}\ (13.48 F_{12\ \mu m} + 5.16 F_{25\ \mu m} + 2.58 F_{60\ \mu m} + F_{100\ \mu m})$, in units of W m$^{-2}$ (Sanders & Mirabel 1996).

the first detection of the $H_2$ $S(0)$ 28.22 $\mu$m transition in the galaxy NGC 6946, using the Short Wavelength Spectrometer (SWS) on the *Infrared Space Observatory* (*ISO*). Subsequently, Rigopoulou et al. (2002) published a survey of $H_2$ in 12 starburst and nine Seyfert galaxies using *ISO*. $H_2$ has been detected in only two ULIRGs, Arp 220 (Sturm et al. 1996) and NGC 6240 (Lutz et al. 2003). A review of the *ISO* $H_2$ observations is given in Habart et al. (2005).

In order to investigate the properties for a statistically representative sample of the local ULIRG population, we have selected 110 ULIRGs with redshifts between 0.02 and 0.93 for observation with *Spitzer*'s Infrared Spectrograph (IRS; Houck et al. 2004), as part of the IRS GTO program. These sources are chosen from the complete Bright Galaxy Sample (Soifer et al. 1987), the 1 Jy (Kim & Sanders 1998) and 2 Jy (Strauss et al. 1992) samples, and the *FIRST*/*IRAS* radio–far-infrared sample of Stanford et al. (2000). Armus et al. (2004) published the first results from this survey for Mrk 1014, Mrk 463, and UGC 5101. Two other papers discussing NGC 6240 and the 10 ULIRGs in the *IRAS* bright galaxy sample (Soifer et al. 1987) are in press (Armus et al. 2006a, 2006b, respectively). In this paper we use the unprecedented sensitivity of the IRS to assess the warm $H_2$ component in a subsample of 77 ULIRGs. All sources were detected at 60 $\mu$m with *IRAS*. Forty-eight of the ULIRGs in our sample are classified as "cold" (i.e., $F_{25\ \mu m}/F_{60\ \mu m} < 0.2$) and likely starburst dominated. The remaining 29 ULIRGs are "warm" (i.e., $F_{25\ \mu m}/F_{60\ \mu m} \geq 0.2$) and are probably powered by an obscured active nucleus. The basic properties of the sample are listed in Table 1.

The *Spitzer* IRS wavelength coverage encompasses the pure rotational $S(0)$ 28.22 $\mu$m through $S(7)$ 5.51 $\mu$m transitions. The relative line strengths allow the determination of the temperature and mass of the warm $H_2$ gas. In § 2 we detail the observations and data reduction, and in § 3 we present the results. In general, the analysis of the warm molecular gas is approximated with a single-temperature model. However, we detected the $S(0)$ line in three ULIRGs, which can lower the derived warm gas temperature. In addition, in some systems we detect the $S(7)$ line, and we use this to model a hot gas component. In the discussion section (§ 4) we investigate the warm gas mass as a function of the average global dust temperature. We also assess the warm gas fraction with respect to the cold gas mass estimates available in the literature. Our conclusions are presented in § 5. Throughout the

TABLE 2

OBSERVATIONAL PARAMETERS

| OBJECT | R.A. (J2000.0) | DECL. (J2000.0) | OBSERVATION DATE | EXECUTION TIME (minutes) | SCALE FACTOR TO *IRAS* 25 $\mu$m FLUX DENSITY | | | | | |
|---|---|---|---|---|---|---|---|---|---|---|
| | | | | | SL2 | SL1 | LL2 | LL1 | SH | LH |
| 3C 273 | 12 29 6.67 | 2 3 8.10 | 2005 Jun 07 | 21.7 | 1.01 | 1.03 | 0.97 | 0.98 | 0.96 | 0.78 |
| Arp 220 | 15 34 57.24 | 23 30 11.70 | 2004 Feb 29 | 42.8 | 1.00 | 1.14 | 0.97 | 0.92 | 1.08 | 1.02 |
| IRAS 00188−08 | 0 21 26.48 | −8 39 27.10 | 2003 Dec 17 | 57.0 | 0.87 | 0.93 | 0.84 | 0.85 | 0.60 | 0.56 |
| IRAS 00275−00 | 0 30 9.09 | −0 27 44.40 | 2005 Jul 08 | 47.2 | 2.33 | 2.16 | 1.88 | 1.70 | ... | ... |
| IRAS 00275−28 | 0 30 4.20 | −28 42 25.40 | 2003 Dec 17 | 28.6 | 0.87 | 0.92 | 0.80 | 0.81 | ... | ... |
| IRAS 00397−13 | 0 42 15.50 | −12 56 3.50 | 2004 Jan 04 | 57.0 | 0.97 | 0.97 | 0.90 | 0.92 | 0.70 | 0.54 |
| IRAS 00406−31 | 0 43 3.14 | −31 10 49.70 | 2005 Jul 11 | 47.2 | 0.95 | 0.99 | 0.93 | 0.94 | ... | ... |
| IRAS 00476−00 | 0 50 9.81 | −0 39 1.00 | 2004 Jul 18 | 67.8 | 0.82 | 0.84 | 0.75 | 0.69 | ... | 0.19 |
| IRAS 01003−22 | 1 2 49.94 | −22 21 57.30 | 2004 Jan 04 | 44.3 | 0.96 | 1.04 | 0.85 | 0.82 | 0.87 | 0.70 |
| IRAS 01199−23 | 1 22 20.84 | −22 51 57.30 | 2004 Jul 18 | 30.4 | 1.08 | 1.16 | 0.96 | 0.92 | ... | ... |
| IRAS 02115+02 | 2 14 10.32 | 2 39 59.80 | 2005 Feb 07 | 23.7 | 0.18 | 0.74 | 0.66 | 0.75 | ... | ... |
| IRAS 02433+01 | 2 45 55.36 | 1 23 28.40 | 2005 Jan 12 | 43.0 | 1.00 | 1.00 | 0.99 | 0.98 | ... | ... |
| IRAS 03521+00 | 3 54 42.15 | 0 37 2.00 | 2004 Feb 27 | 57.2 | 0.90 | 0.90 | 0.80 | 0.81 | 0.42 | 0.48 |
| IRAS 04114−51 | 4 12 44.92 | −51 9 34.20 | 2004 Aug 11 | 28.5 | 0.98 | 1.02 | 0.97 | 1.02 | ... | ... |
| IRAS 04313−16 | 4 33 37.08 | −16 43 31.50 | 2004 Mar 01 | 35.8 | 0.94 | 1.14 | 0.91 | 0.92 | ... | ... |
| IRAS 05189−25 | 5 21 1.41 | −25 21 45.50 | 2004 Mar 22 | 41.2 | 1.05 | 1.09 | 1.00 | 1.01 | 1.07 | 1.07 |
| IRAS 06035−71 | 6 2 53.63 | −71 3 11.90 | 2004 Apr 14 | 42.9 | 1.37 | 1.47 | 1.17 | 1.07 | 1.73 | 1.07 |
| IRAS 06206−63 | 6 21 0.80 | −63 17 23.20 | 2004 Apr 16 | 44.1 | 0.91 | 0.96 | 0.84 | 0.78 | 1.05 | 0.79 |
| IRAS 06301−79 | 6 26 42.20 | −79 36 30.40 | 2004 Aug 11 | 28.5 | 1.00 | 1.09 | 0.92 | 0.95 | ... | ... |
| IRAS 06361−62 | 6 36 35.71 | −62 20 31.80 | 2004 Aug 11 | 30.4 | 0.94 | 0.97 | 0.96 | 0.98 | ... | ... |
| IRAS 07598+65 | 8 4 30.46 | 64 59 52.90 | 2004 Feb 29 | 43.2 | 1.08 | 1.11 | 1.01 | 0.98 | 1.05 | 0.92 |
| IRAS 08311−24 | 8 33 20.47 | −25 9 33.10 | 2004 Apr 14 | 42.9 | ... | ... | ... | ... | 1.68 | 1.16 |
| IRAS 08572+39 | 9 0 25.38 | 39 3 54.30 | 2004 Apr 15 | 42.3 | 1.05 | 1.13 | 1.00 | 0.91 | 1.05 | 0.89 |
| IRAS 09022−36 | 9 4 12.69 | −36 27 1.70 | 2005 Jun 07 | 37.8 | ... | ... | ... | ... | ... | ... |
| IRAS 09463+81 | 9 53 0.09 | 81 27 28.20 | 2004 Mar 23 | 28.5 | 1.27 | 1.29 | 0.94 | 0.95 | ... | ... |
| IRAS 10091+47 | 10 12 16.74 | 46 49 42.90 | 2004 Apr 19 | 28.5 | 0.87 | 0.88 | 0.84 | 0.85 | ... | ... |
| IRAS 10398+32 | 10 42 40.81 | 32 31 31.00 | 2004 Dec 08 | 42.9 | 0.85 | 0.81 | 0.02 | 0.76 | ... | ... |
| IRAS 10565+24 | 10 59 18.14 | 24 32 34.30 | 2004 May 12 | 42.8 | 1.22 | 1.32 | 1.11 | 1.03 | 1.12 | 0.97 |
| IRAS 11119+32 | 11 14 38.88 | 32 41 33.10 | 2004 May 11 | 52.0 | 1.20 | 1.57 | 1.00 | 1.01 | 1.10 | 0.86 |
| IRAS 12018+19 | 12 4 24.53 | 19 25 9.80 | 2004 May 15 | 51.9 | 1.06 | 1.10 | 0.92 | 0.92 | 0.87 | 0.76 |
| IRAS 12032+17 | 12 5 47.73 | 16 51 8.20 | 2004 Jan 04 | 28.6 | 1.22 | 1.27 | 1.00 | 0.95 | ... | ... |
| IRAS 12072−04 | 12 9 45.12 | −5 1 13.90 | 2004 Jan 06 | 44.3 | 1.16 | 1.23 | 1.11 | 1.12 | 0.99 | 0.88 |
| IRAS 12112+03 | 12 13 46.05 | 2 48 41.30 | 2004 Jan 04 | 44.0 | 1.33 | 1.37 | 1.24 | 1.25 | 1.12 | 0.93 |
| IRAS 12514+10 | 12 54 0.82 | 10 11 12.40 | 2005 Feb 06 | 62.7 | 0.96 | 0.98 | 0.92 | 0.91 | 0.77 | 0.60 |
| IRAS 13120−54 | 13 15 6.40 | −55 9 23.30 | 2004 Mar 02 | 40.1 | 1.38 | 1.49 | 1.07 | 1.02 | 1.24 | 1.09 |
| IRAS 13218+05 | 13 24 19.81 | 5 37 4.60 | 2004 Jul 17 | 51.7 | 0.97 | 0.99 | 0.91 | 0.91 | ... | 0.60 |
| IRAS 13342+39 | 13 36 24.07 | 39 17 30.10 | 2004 May 12 | 64.1 | 1.07 | 1.07 | 0.97 | 0.94 | ... | 0.88 |
| IRAS 13352+64 | 13 36 51.15 | 63 47 4.70 | 2005 Mar 20 | 47.2 | 0.99 | 0.96 | 0.94 | 0.94 | ... | ... |
| IRAS 13451+12 | 13 47 33.36 | 12 17 24.20 | 2004 Jan 07 | 42.9 | 1.21 | 1.29 | 1.19 | 1.21 | 1.11 | 1.02 |
| IRAS 14348−14 | 14 37 38.27 | −15 0 24.60 | 2004 Feb 07 | 44.4 | 1.07 | 1.25 | 1.17 | 1.13 | 0.99 | 0.81 |
| IRAS 14378−36 | 14 40 58.90 | −37 4 33.00 | 2004 Mar 02 | 43.2 | 1.70 | 1.51 | 1.25 | 1.19 | 1.62 | 1.02 |
| IRAS 14537+19 | 14 56 4.43 | 19 38 45.70 | 2004 Jul 14 | 67.5 | 0.85 | 0.85 | 0.77 | 0.74 | ... | 0.22 |
| IRAS 14548+33 | 14 56 58.43 | 33 37 10.00 | 2005 Mar 17 | 43.1 | 0.63 | 0.96 | 0.91 | 0.84 | ... | ... |
| IRAS 15001+14 | 15 2 31.94 | 14 21 35.30 | 2004 Jun 27 | 56.9 | 1.09 | 1.25 | 0.96 | 0.95 | ... | 0.79 |
| IRAS 15206+33 | 15 22 38.12 | 33 31 36.10 | 2004 Jun 24 | 51.8 | 1.01 | 1.07 | 0.83 | 0.83 | ... | 0.78 |
| IRAS 15250+36 | 15 26 59.40 | 35 58 37.50 | 2004 Mar 04 | 43.4 | 1.03 | 1.00 | 0.97 | 0.92 | 1.01 | 0.92 |
| IRAS 15462−04 | 15 48 56.80 | −4 59 33.70 | 2004 Mar 02 | 52.1 | 1.23 | 1.35 | 1.04 | 1.00 | 0.96 | 0.83 |
| IRAS 16124+32 | 16 14 22.11 | 32 34 3.70 | 2005 Mar 19 | 48.0 | 0.41 | 0.92 | 0.88 | 0.87 | ... | ... |
| IRAS 16334+46 | 16 34 52.37 | 46 24 53.00 | 2004 Mar 04 | 28.8 | 0.83 | 0.35 | 0.65 | 0.63 | ... | ... |
| IRAS 17068+40 | 17 8 32.12 | 40 23 28.20 | 2004 Apr 16 | 30.4 | 0.89 | 0.90 | 0.90 | 0.93 | ... | ... |
| IRAS 17179+54 | 17 18 54.23 | 54 41 47.30 | 2004 Apr 17 | 66.6 | 1.14 | 1.25 | 1.08 | 1.04 | 1.18 | 1.07 |
| IRAS 17208−00 | 17 23 21.93 | −0 17 0.40 | 2004 Mar 27 | 42.2 | 1.33 | 1.35 | 1.17 | 1.07 | 1.19 | 1.03 |
| IRAS 17233+37 | 17 25 7.40 | 37 9 32.10 | 2004 Jun 06 | 67.6 | 0.25 | 1.12 | 1.12 | 0.95 | ... | 0.94 |
| IRAS 17463+58 | 17 47 4.76 | 58 5 22.10 | 2004 Apr 17 | 32.8 | 0.96 | 0.96 | 0.91 | 0.92 | ... | ... |
| IRAS 18030+07 | 18 5 32.50 | 7 6 9.00 | 2004 Mar 25 | 28.5 | 0.87 | 0.93 | 0.78 | 0.75 | ... | ... |
| IRAS 18443+74 | 18 42 54.80 | 74 36 21.00 | 2004 Mar 05 | 30.7 | 1.01 | 0.97 | 0.94 | 0.95 | ... | ... |
| IRAS 19254−72 | 19 31 21.55 | −72 39 22.00 | 2005 May 30 | 37.7 | ... | ... | ... | ... | 6.62 | 1.31 |
| IRAS 19297−04 | 19 32 21.25 | −3 59 56.30 | 2004 May 13 | 42.7 | 0.95 | 0.97 | 0.84 | 0.82 | ... | 0.71 |
| IRAS 19458+09 | 19 48 15.70 | 9 52 5.00 | 2004 Apr 18 | 30.4 | 1.15 | 1.14 | 1.05 | 0.96 | ... | ... |
| IRAS 20037−15 | 20 6 31.70 | −15 39 8.00 | 2004 Apr 18 | 28.5 | 1.16 | 1.26 | 0.96 | 0.94 | ... | ... |
| IRAS 20087−03 | 20 11 23.86 | −2 59 50.80 | 2004 May 14 | 49.1 | 0.99 | 0.96 | 0.87 | 0.86 | ... | 0.62 |
| IRAS 20100−41 | 20 13 29.85 | −41 47 34.70 | 2004 Apr 13 | 44.1 | 0.89 | 0.90 | 0.86 | 0.82 | 0.70 | 0.70 |
| IRAS 20414−16 | 20 44 18.18 | −16 40 16.40 | 2004 May 14 | 44.1 | 1.06 | 1.07 | 0.88 | 0.83 | ... | 0.55 |
| IRAS 20551−42 | 20 58 26.78 | −42 39 1.60 | 2004 May 14 | 39.7 | 1.07 | 1.11 | 0.97 | 0.92 | ... | 0.85 |

TABLE 2—*Continued*

| Object | R.A. (J2000.0) | Decl. (J2000.0) | Observation Date | Execution Time (minutes) | Scale Factor to *IRAS* 25 $\mu$m Flux Density | | | | | |
|---|---|---|---|---|---|---|---|---|---|---|
| | | | | | SL2 | SL1 | LL2 | LL1 | SH | LH |
| IRAS 21272+25 | 21 29 29.40 | 25 27 55.10 | 2004 Jun 24 | 30.4 | 1.16 | 1.18 | 1.12 | 1.13 | ... | ... |
| IRAS 22491−18 | 22 51 49.35 | −17 52 24.00 | 2004 Jun 24 | 44.2 | 1.37 | 1.38 | 1.11 | 1.11 | ... | 0.99 |
| IRAS 23128−59 | 23 15 47.01 | −59 3 16.90 | 2004 May 11 | 42.4 | 1.59 | 1.73 | 1.43 | 1.38 | ... | 1.11 |
| IRAS 23129+25 | 23 15 21.41 | 26 4 32.60 | 2003 Dec 17 | 40.6 | 0.92 | 0.92 | 0.92 | 0.91 | ... | ... |
| IRAS 23365+36 | 23 39 1.29 | 36 21 9.80 | 2004 Jan 08 | 43.1 | 2.90 | 2.68 | 1.31 | 1.17 | 2.33 | 1.08 |
| IRAS 23498+24 | 23 52 26.05 | 24 40 16.20 | 2004 Jan 04 | 64.1 | 0.97 | 1.03 | 0.81 | 0.84 | 0.68 | 0.53 |
| IRAS 23529−21 | 23 55 33.22 | −21 2 59.60 | 2003 Dec 16 | 40.6 | 1.00 | 0.99 | 0.87 | 0.82 | ... | ... |
| Mrk 1014 | 1 59 50.23 | 0 23 40.50 | 2004 Jan 07 | 43.0 | 1.17 | 1.32 | 1.09 | 1.04 | 1.08 | 0.86 |
| Mrk 231 | 12 56 14.29 | 56 52 25.10 | 2004 Apr 14 | 41.0 | 1.20 | 1.17 | 1.03 | 1.03 | 1.18 | 1.09 |
| Mrk 273 | 13 44 42.12 | 55 53 13.10 | 2004 Apr 14 | 39.8 | 1.18 | 1.19 | 1.06 | 1.06 | 1.24 | 1.07 |
| Mrk 463E | 13 56 2.90 | 18 22 19.00 | 2004 Jan 07 | 42.5 | 1.00 | 1.02 | 0.97 | 1.01 | 0.99 | 0.97 |
| NGC 6240 | 16 52 58.89 | 2 24 3.40 | 2004 Mar 04 | 40.0 | 0.93 | 1.08 | 1.00 | 1.01 | 1.10 | 1.03 |
| UGC 5101 | 9 35 51.65 | 61 21 11.30 | 2004 Mar 23 | 42.7 | 1.11 | 1.19 | 1.13 | 1.15 | 1.19 | 1.10 |

Note.—Units of right ascension are hours, minutes, and seconds, and units of declination are degrees, arcminutes, and arcseconds.

paper we adopt a flat $\Lambda$-dominated universe ($H_0 = 71$ km s$^{-1}$ Mpc$^{-1}$, $\Omega_M = 0.27$, $\Omega_\Lambda = 0.73$, and $\Omega_k = 0$).

## 2. OBSERVATIONS AND DATA REDUCTION

The data presented here were obtained using the IRS. In low-resolution mode (IRS-LORES) there are two spectrometers with a resolving power $64 \leq \lambda/\Delta\lambda \leq 128$. Short-Low (IRS-SL) operates between 5.2 and 7.7 $\mu$m in Short-Low 2 (IRS-SL2) and 7.4–14.5 $\mu$m in Short-Low 1 (IRS-SL1). Long-Low (IRS-LL) gives coverage from 14.0 to 21.3 $\mu$m in Long-Low 2 (IRS-LL2) and 19.5 to 38.0 $\mu$m in Long-Low 1 (IRS-LL1). The two high-resolution spectrometers (IRS-HIRES) have a resolving power $\lambda/\Delta\lambda \sim 600$. Short-High (IRS-SH) encompasses the range 9.9–19.6 $\mu$m, and Long-High (IRS-LH) spans 18.7–37.2 $\mu$m. The observations were made in the IRS Staring Mode Astronomical Observing Template (AOT). A high-accuracy blue peak-up, using either a star from the Two Micron All Sky Survey (2MASS) catalog (Cutri et al. 2003) or the source itself, was executed in order to accurately place our targets on the IRS slits. The observation log is given in Table 2. The IRS is fully described in Houck et al. (2004), and the observing mode details are presented in the *Spitzer* Observers Manual (SOM).[5]

The spectral data were processed as far as the un–flat-fielded two-dimensional image using the standard IRS S11 pipeline (see the SOM). The spectra were then extracted and sky subtracted using the SMART analysis package (Higdon et al. 2004). To maximize the signal-to-noise ratio (S/N) in the final spectra the data were extracted using a column whose width in the cross-dispersion direction scales with the instrument point-spread function (PSF). The spectra were flat-fielded and flux-calibrated by extracting and sky-subtracting un–flat-fielded observations of the calibration stars, HR 6348 (IRS-SL), HD 173511 (IRS-LL), and HD 163588 (IRS-HIRES), and dividing these data by their respective templates (Cohen et al. 2003) to generate a one-dimensional relative spectral response function (RSRF). The RSRF was then applied to the TARGET observations to produce the final spectra. The residual sky was subtracted from the IRS-LORES data using the off-source observations, which are part of the staring mode AOT. For the IRS-HIRES data, a spectrum of the zodiacal light on the date of the observation was generated using the Spitzer Planning and Observation Tool (SPOT; this uses the zodiacal light model of Reach et al. 2003), scaled using the IRS-HIRES apertures, and subtracted from the spectra. The IRS-HIRES spectra were defringed in SMART. The spectra were scaled to match the 25 $\mu$m flux densities measured by *IRAS*. Sources lacking a measured *IRAS* 25 $\mu$m flux density were observed with the IRS peak-up arrays, allowing us to scale the spectra to match the source's 22 $\mu$m flux density. The scaling factors, which are multiplicative, are listed in Table 2. The ULIRG IRAS 09022−36 required an extremely large scaling factor ($\sim$17) to bring the SH and 25 $\mu$m flux density measured by *IRAS* into agreement. We chose not to scale the data. We are confident in the detection of the *S*(1) line. However, the absolute flux calibration of this source is uncertain.

Most of the mid-infrared emission in ULIRGs arises in a region of the order of 1 to a few kiloparsecs in size, which are spatially unresolved with respect to the IRS slits.[6] To check this assumption we examined the IRS-SL2 data. This has the highest spatial resolution, with 1.″8 pixel$^{-1}$. The IRS-SL2 data were collapsed in the dispersion direction, and a Gaussian was fit to the profile. Our calibration star, HR 6348, is fit with a Gaussian, with a FWHM of 2.″88. Only IRAS 09022−3615, IRAS 12112+0305, and IRAS 14348−1447 show evidence of significant source extension, i.e., FWHM $\geq 1.5\,\mathrm{FWHM_{star}}$. Their FWHMs are 3.0, 1.7, and 1.7 times that of the calibration star, respectively. Both IRAS 12112+0305 and IRAS 14348−1447 are known doubles with nuclei separated by 2.9 and 3.4″, respectively, and the 5″ Gaussian FWHM corresponds to a linear diameter of 8 and 9 kpc, respectively. Our observations were centered on the northeast nucleus in IRAS 12112+0305 and the southwest nucleus in IRAS 14348−1447, as these are the dominant nuclei in the near-infrared and in CO (Evans et al. 2000, 2002). For IRAS 09022−3615 there was a pointing problem, and the PSF is poorly sampled. No additional correction to line fluxes has been made to account for the extended emission.

Blending is a problem for the higher rotational lines, which can only be observed with the IRS-LORES. The *S*(6) 6.1 $\mu$m line, for example, can be blended with polycyclic aromatic hydrocarbon (PAH) emission at 6.2 $\mu$m, the *S*(5) 6.9 $\mu$m line can be blended with the [Ar II] 7.0 $\mu$m line and PAH emission at 7.0 $\mu$m, and the *S*(4) 8.0 $\mu$m line can be blended with PAH emission at 7.8 and 8.3 $\mu$m. NGC 6240 is the only source in our sample where the emission is bright enough to be detected in these transitions (Armus et al. 2006a).

[5] See http://ssc.spitzer.caltech.edu/documents/som, chap. 7.

[6] The slit sizes for the IRS modules are SL2: 3.″6 × 57″, SL1: 3.″7 × 57″, LL2: 10.″5 × 168″, LL1: 10.″7 × 168″, SH: 4.″7 × 11.″3, LH: 11.″1 × 22.″3.

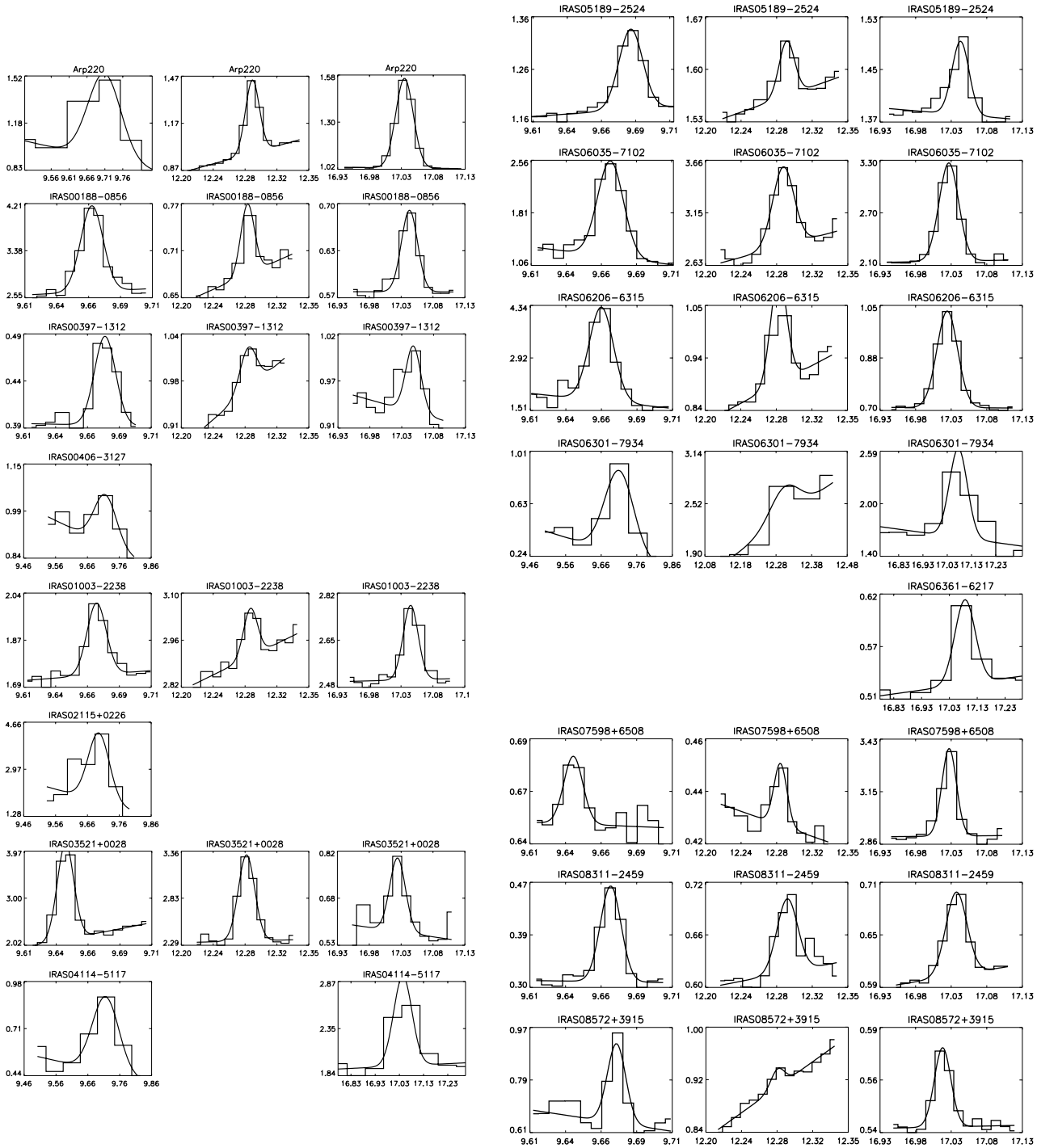


FIG. 1.—Pure rotational $H_2$ emission lines for the ULIRG sample observed with *Spitzer*'s IRS. The three columns show (*from left to right*) the $H_2$ $S(3)$ 9.67 $\mu$m, $S(2)$ 12.28 $\mu$m, and $S(1)$ 17.04 $\mu$m lines after averaging over both slit positions. The data are shown as a histogram, while the solid line shows a single Gaussian plus linear baseline fit. The vertical axis shows flux density in units of $10^{-18}$ W cm$^{-2}$ $\mu$m$^{-1}$, with rest wavelength in microns shown on the horizontal axis.

The resulting $S(3)$, $S(2)$, and $S(1)$ $H_2$ line profiles, averaged over the two slit-nod positions, are shown in the first, second, and third columns of Figure 1, respectively. The $S(0)$ detections, which indicate a somewhat cooler $H_2$ component, are shown in Figure 2, while the $S(7)$ detections, which arise from a hotter $H_2$ component, are shown in Figure 3. In Table 3 we list the line fluxes and upper limits. We find the dominant source of uncertainty in the line fluxes to be the difference between the fits to the line profiles in the two slit-nod positions. Upper limits are calculated using the residuals (rms) from a zeroth-order fit to the continuum. We take the 3 $\sigma$ upper limit to be $3 \times \mathrm{rms} \times \mathrm{FWHM}$. No extinction correction has been applied to the observed line fluxes. Determining the correct extinction factor is inherently difficult, and we address this in § 3.2, where we discuss the location of the warm molecular hydrogen gas. We calculate a lower limit to the fraction of the total far-infrared luminosity, $L_{\mathrm{IR}}$,[7] radiated in the $H_2$ for those sources that have at least one measured emission-line flux. The lower limit is the sum of the line luminosities that

[7] $L_{\mathrm{IR}} = L_{8-1000\ \mu\mathrm{m}}$ is defined to be $4\pi d_L^2 F_{\mathrm{IR}}$ in units of $L_\odot$, where $d_L$ is the luminosity distance and $F_{\mathrm{IR}} = 1.8 \times 10^{-14}\,(13.48F_{12\ \mu\mathrm{m}} + 5.16F_{25\ \mu\mathrm{m}} + 2.58F_{60\ \mu\mathrm{m}} + F_{100\ \mu\mathrm{m}})$ in W m$^{-2}$ (Sanders & Mirabel 1996).

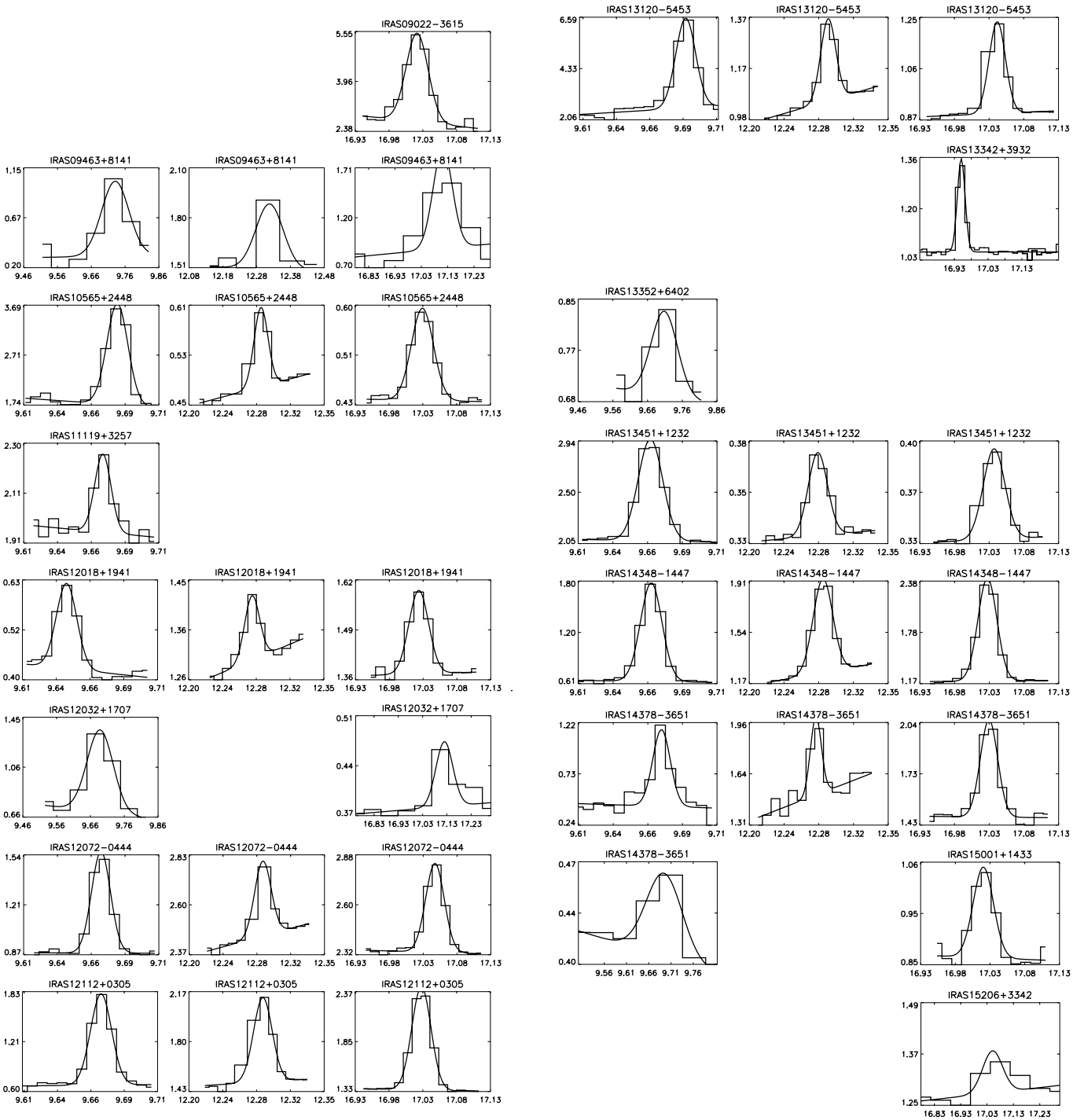


FIG. 1.—*Continued*

were fit with a Gaussian, divided by $L_{IR}$. Typically, ~0.01% of the total far-infrared luminosity is radiated in the $H_2$ rotational lines.

## 3. RESULTS

Before deriving the physical properties of the warm molecular hydrogen, we take a quick look at the sample to check for systematic offsets and biases. All 77 ULIRGs were observed using IRS-LORES. However, the brighter sources were also observed in IRS-HIRES, 15 with IRS-LH and 37 with both IRS-SH and IRS-LH. We find no significant difference in the $H_2$ detection rate for these IRS-LORES and IRS-HIRES observations. For IRS-HIRES the detection rate is 35 of 50 (70% ± 12%) as compared to 51 of 77 (66% ± 9%) for IRS-LORES observations. Twenty-five sources have both IRS-LORES and IRS-HIRES measurements of the *S*(1) line. On average, the IRS-HIRES measurement is 90% ± 31% of the IRS-LORES value. Twenty-three sources have both IRS-LORES and IRS-HIRES measurements of the *S*(3) line. Two sources, IRAS 08311−2459 and IRAS 19254−7245, have large line flux uncertainties. The remaining 21 sources have an average IRS-HIRES measurement that is 100% ± 33% of the average IRS-LORES line flux. There is no evidence for a significant systematic difference between high- and low-resolution line flux measurements.

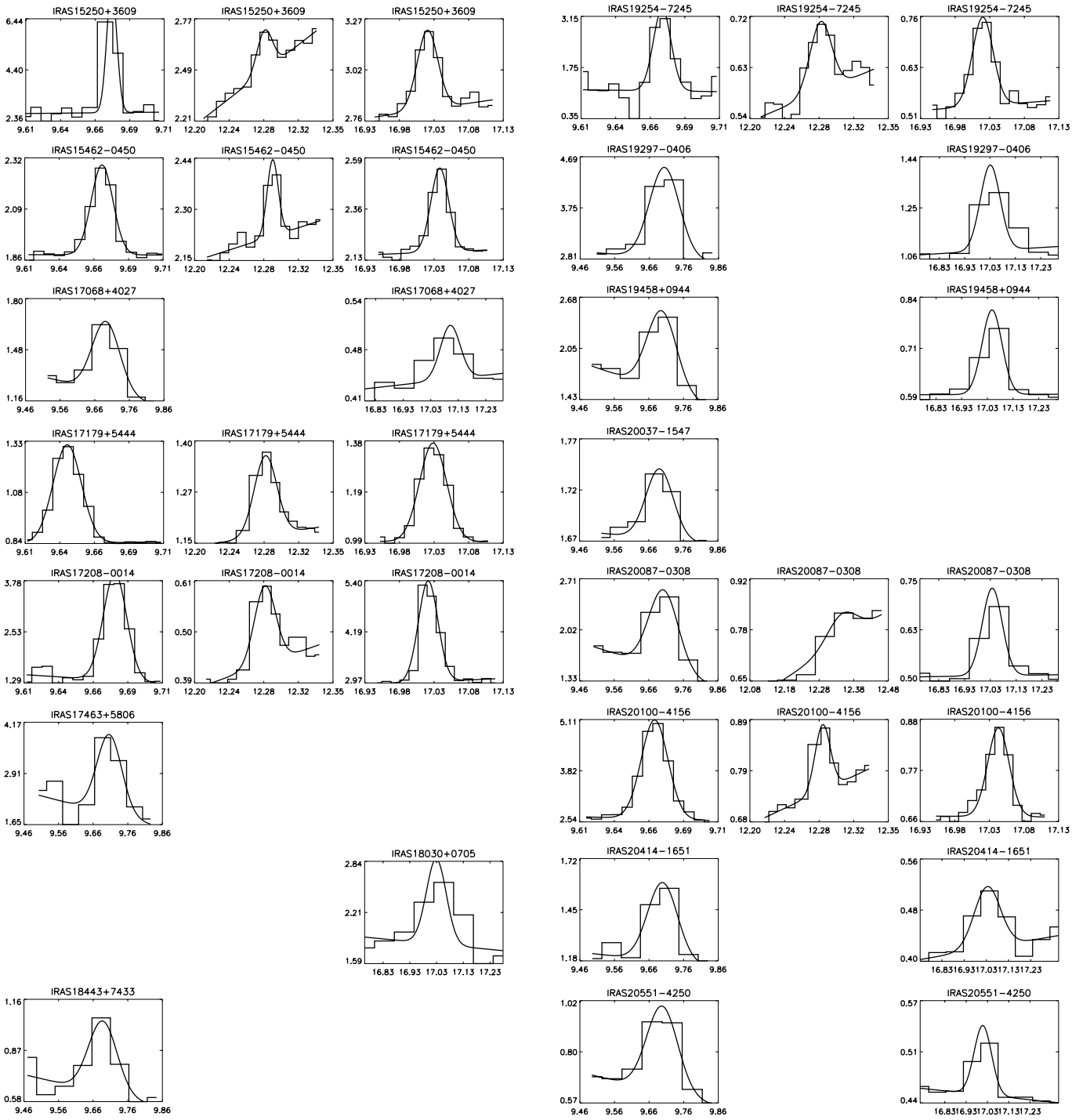


FIG. 1.—*Continued*

The sample contains a mixture of warm and cold sources. Nineteen of the 29 warm ULIRGs were detected in $H_2$ (65% ± 15%), whereas 40 of the 48 cold ULIRGs were detected (83% ± 13%). There is thus no significant statistical difference in the detection rate for the two subpopulations.

The likelihood for detecting $H_2$ is flux limited. There are 40 sources in our sample that have an *IRAS* 60 $\mu$m flux density $\leq$2 Jy. This includes the 18 sources in the sample for which we do not detect any molecular hydrogen emission and 12 of the 16 sources for which we only detect a single emission line. This suggests a detection limit based on our choice of integration time. We detect molecular hydrogen in all sources with 60 $\mu$m flux densities >2 Jy, irrespective of the warm/cold classification.

### 3.1. *Warm* $H_2$ *Gas*

To derive the mass of warm molecular hydrogen we assume that all of our sources are spatially unresolved by the IRS and that the emission is optically thin. The critical densities of the $J = 2$, 3, and 4 levels are relatively low ($n_{cr} < 10^3$ cm$^{-3}$), and we assume that the populations are in LTE. Adopting an ortho-to-para ratio of 3, we constructed an excitation diagram for each source.[8] This is simply the natural logarithm of the number of molecules divided by the statistical weight in the upper level of each

[8] The complete set of excitation diagrams is available at http://isc.astro.cornell.edu/~sjuh/ulirgs/h2/excitation-diagrams.html.

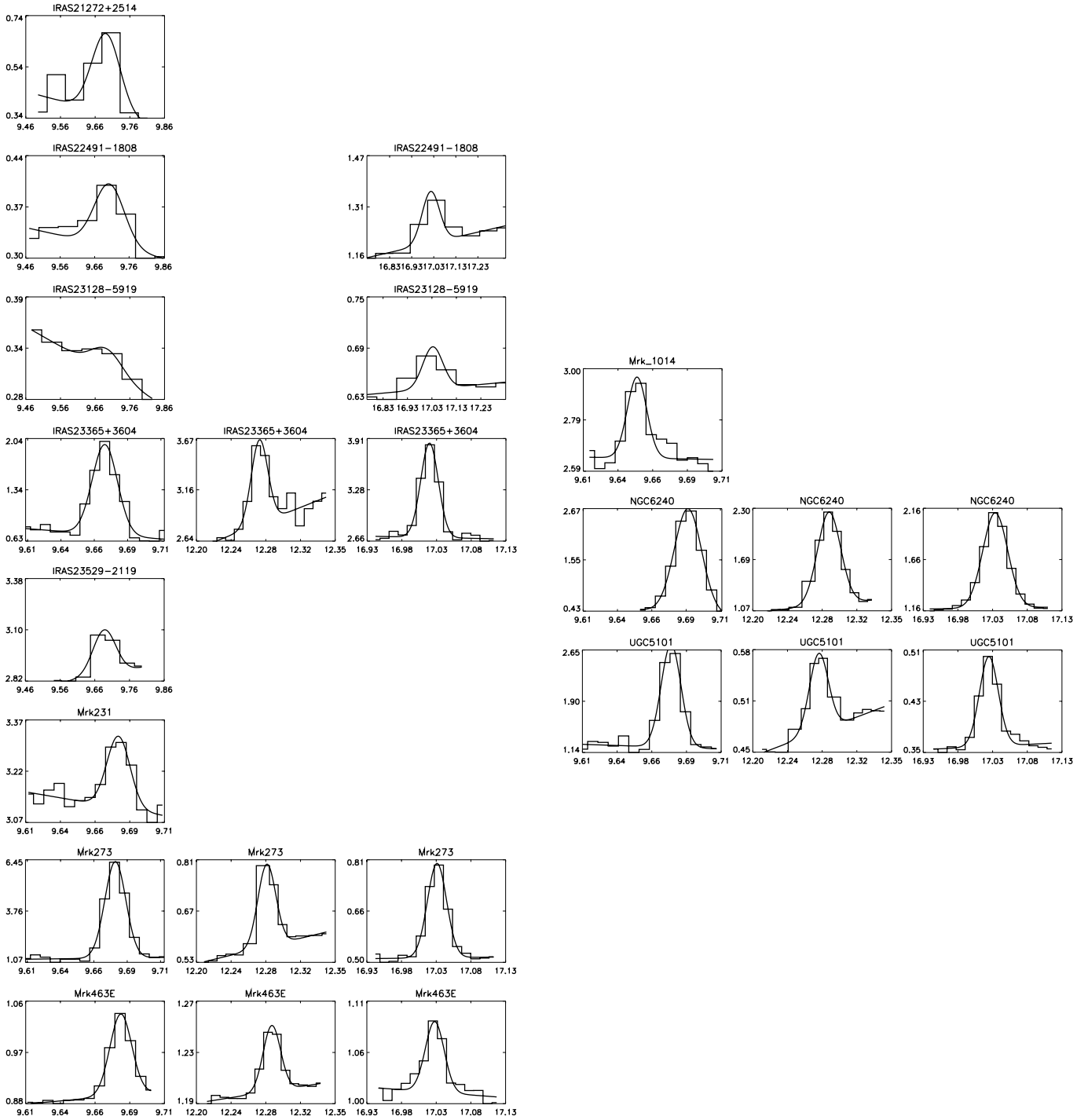


FIG. 1.—*Continued*

transition versus the energy level. If the $H_2$ is characterized by a single temperature, the data will lie on a straight line, with the excitation temperature ($T_{ex}$) being the reciprocal of the slope. The excitation diagram for IRAS 00188−0856 is shown in Figure 4. This is a typical example of single-component fit, which is the case for the majority of our sources. The mass of warm $H_2$ can be derived from the line luminosity and the excitation temperature. For example, using the luminosity of the $S(1)$ 17.04 $\mu$m (ortho) line, the energy of a given level is given by $E_J = 85kJ(J+1)$, where $k$ is the Boltzmann constant. The total mass ($M_{tot}$) is $\frac{4}{3}M_o$, where $M_o$ is the mass of gas in the ortho state and $M_o = m_{H_2}N_T$, with $m_{H_2}$ being the molecular mass of $H_2$ and $N_T$ being the total number of molecules. However, $N_T = N_J/f_J$, where $N_J$ is the number of molecules in the $J$th state, $N_J = [L(J)]/(A_J\Delta E_J)$. Here $L(J)$ is the line luminosity, $A_J$ is the Einstein $A$-coefficient, and $\Delta E_J = h\nu_J$, where $h$ is Planck's constant and $\nu_J$ is the frequency of the emission line; $f_J$ is the partition function for the $J$th state, $f_J = \{g_J \exp[-(E_J/kT_{ex})]\}/\{\sum_{J',\text{ortho}} g_{J'} \exp[-(E_{J'}/kT_{ex})]\}$, where $g_J$ is the statistical weight for a given state.

We derived an excitation temperature for approximately half of our ULIRG sample (43 sources) that had detections in at least two transitions. The mean $T_{ex}$ for this subsample is $336 \pm 15$ K. Table 3 also lists an additional 16 sources in which we only see a

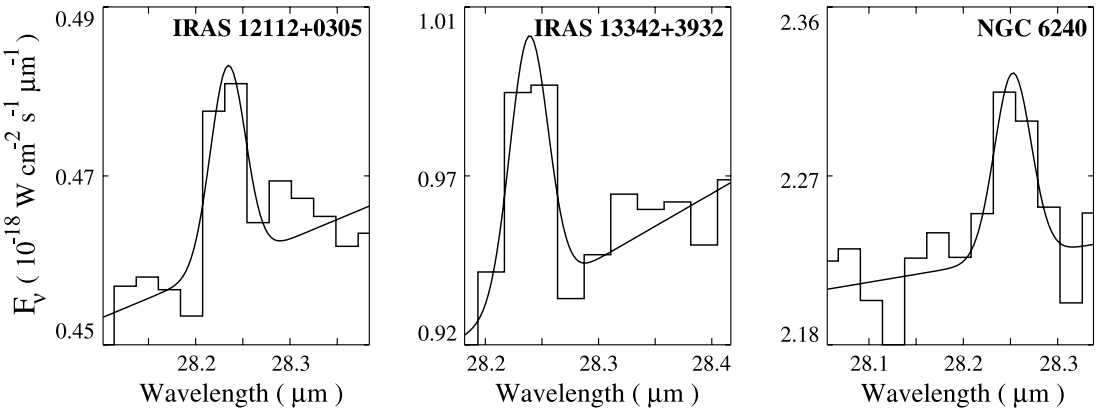


FIG. 2.—Observed (*histogram*) and fitted (*line*) $H_2$ $S(0)$ 28.22 $\mu$m lines detected with the IRS in the ULIRGs IRAS 12112+0305, IRAS 13342+3932, and NGC 6240. The spectra represent averages of the two slit positions. The vertical axis shows flux density in units of $10^{-18}$ W cm$^{-2}$ s$^{-1}$ $\mu$m$^{-1}$, while the horizontal axis shows the rest wavelength in microns.

single ortho–molecular hydrogen line. We used the mean $T_{ex}$ to estimate the warm gas mass in these sources. The warm gas masses range from $10^7$ to $10^9$ $M_\odot$, with an average value of $\sim 2 \times 10^8$ $M_\odot$. The warm molecular hydrogen excitation temperatures and masses are given in Table 4.

### 3.2. *Extinction and the Ortho-to-Para Ratio*

It is inherently difficult to derive the correct extinction along a given line of sight. Using optical depths derived in the mid-infrared alleviates the problem of extrapolating from a measurement made in the optical. However, the geometry of the emitting sources and whether the derived optical depth should be approximated as a foreground screen or material mixed with the warm gas, in either a clumpy or a uniform medium, are all highly uncertain. Figure 5 shows the combined low-resolution and high-resolution spectrum of Mrk 273 from 6.5 to 13.5 $\mu$m. The deep silicate absorption feature corresponds to an optical depth of $\tau_{9.7\,\mu m} \sim 2$, implying an $A_V \sim 20$–$40$ (Roche & Aitken 1985). For molecular hydrogen at a temperature of 380 K in LTE with an ortho-to-para ratio of 3, the intrinsic $S(2)/S(3)$ line ratio is 0.56. If the $H_2$ has the same extinction implied by the depth of the silicate absorption trough, the line ratio will be in the range 1.05–1.95 when the absorbing material is in a foreground screen, and 0.74–0.90 for a mixture of dust and gas. The observed $S(2)/S(3)$ line ratio is $0.54 \pm 0.08$, which is consistent with the unextincted value. In Figure 6 we plot $T_{ex}$ versus the observed $H_2$ $S(1)/S(3)$ line ratio, which is independent of the ortho-to-para ratio. The data represent the 27 galaxies where at least three $J \leq 4$ lines are detected in the IRS-HIRES observations. NGC 6240 and IRAS 12112+0305 are not included in this selection, as their excitation diagrams are best described by multicomponent gas, as we describe more fully in the next section. The figure shows that the majority of the sources have line ratios that are consistent with the theoretical value for no extinction. From this we infer that the absorbing material along the line of sight to the central AGN does not lie in a screen between us and the warm molecular gas. If the $H_2$ emission originates from a massive and dusty circumnuclear torus, then the gas and dust are mixed, and the bulk of the emission must arise from regions with optical depths less than 3, as described by Burton et al. (1992). Alternately, the $H_2$ emission may

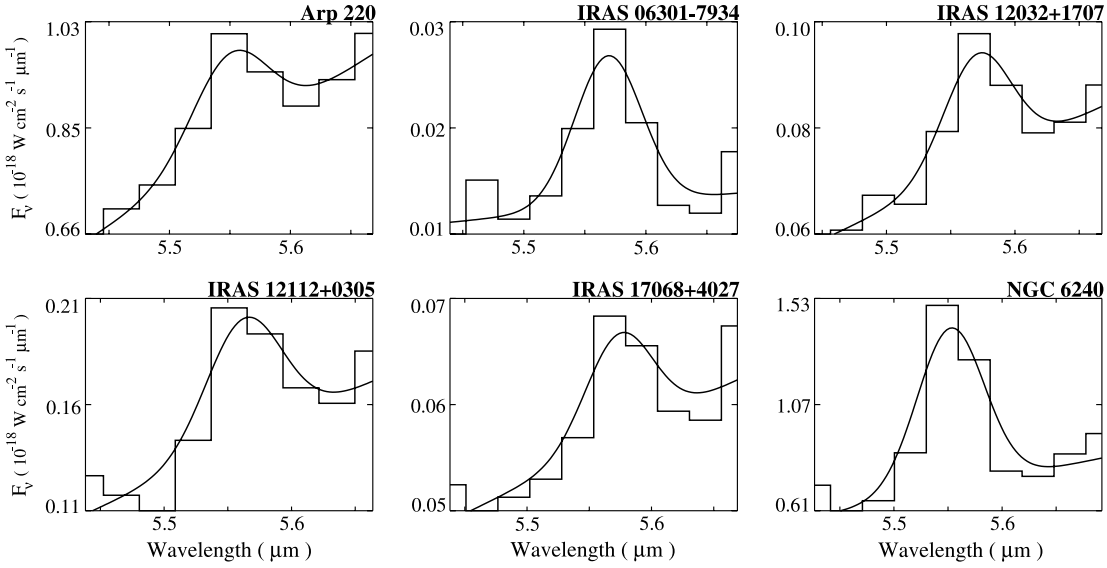


FIG. 3.—Observed (*histogram*) and fitted (*line*) $H_2$ $S(7)$ 5.51 $\mu$m emission lines detected with the IRS in the ULIRGs Arp 220, IRAS 06301−79304, IRAS 12032+1707, IRAS 12112+0305, IRAS 17068+4027, and NGC 6240. The spectra represent averages of both slit positions. The vertical axis shows flux density in units of $10^{-18}$ W cm$^{-2}$ $\mu$m$^{-1}$. Rest wavelength in microns is shown along the horizontal axis.

TABLE 3

MEASURED LINE FLUXES AND LIMITS

| Object | $S(0)$ 28.22 $\mu$m ($10^{-20}$ W cm$^{-2}$) | $S(1)$ 17.04 $\mu$m ($10^{-20}$ W cm$^{-2}$) | $S(2)$ 12.28 $\mu$m ($10^{-20}$ W cm$^{-2}$) | $S(3)$ 9.67 $\mu$m ($10^{-20}$ W cm$^{-2}$) | $S(7)$ 5.51 $\mu$m ($10^{-20}$ W cm$^{-2}$) | $L_{H_2}/L_{IR}$[a] (%) |
|---|---|---|---|---|---|---|
| 3C 273 | <2.2 | <3.5 | <3.2 | <3.6 | <27.3 | ... |
| Arp 220 | <97.0 | 1.862 ± 0.168 | 0.98 ± 0.13 | 0.73 ± 0.02[b] | 1.29 ± 0.38 | 0.006 |
| IRAS 00188−0856 | <1.9 | 0.043 ± 0.005 | 0.020 ± 0.004 | 0.038 ± 0.012 | <3.2 | 0.004 |
| IRAS 00275−0044 | <3.7[b] | <1.2[b] | <1.1[b] | <0.5[b] | <0.8 | ... |
| IRAS 00275−2859 | <5.4[b] | <3.1[b] | <2.6[b] | <2.7[b] | <3.0 | ... |
| IRAS 00397−1312 | <1.6 | 0.029 ± 0.004 | 0.017 ± 0.002 | 0.023 ± 0.006 | <8.0 | 0.006 |
| IRAS 00406−3127 | <5.1[b] | <1.5[b] | <1.2[b] | 0.019 ± 0.001[b] | <1.0 | 0.003 |
| IRAS 00476−0054 | ... | <0.1 | <0.4[b] | <0.3[b] | <0.2 | ... |
| IRAS 01003−2238 | <3.5 | 0.087 ± 0.031 | 0.034 ± 0.002 | 0.057 ± 0.007 | <2.5 | 0.008 |
| IRAS 01199−2307 | <10.6[b] | <1.5[b] | <1.2[b] | <0.1[b] | <0.5 | ... |
| IRAS 02115+0226 | ... | <0.2[b] | <0.2[b] | 0.029 ± 0.002[b] | <0.03 | 0.004 |
| IRAS 02433+0110 | ... | <1.0[b] | <0.8[b] | <0.6[b] | <0.4 | ... |
| IRAS 03521+0028 | <1.3 | 0.082 ± 0.013 | 0.027 ± 0.009 | 0.037 ± 0.003 | <0.3 | 0.006 |
| IRAS 04114−5117 | <8.7[b] | 0.104 ± 0.010[b] | <0.6[b] | 0.051 ± 0.019[b] | <0.4 | 0.009 |
| IRAS 04313−1649 | <6.6[b] | <0.9[b] | <0.5[b] | <0.1[b] | <0.2 | ... |
| IRAS 05189−2524 | <28.2 | 0.34 ± 0.07 | 0.15 ± 0.02 | 0.36 ± 0.13 | <34.1 | 0.003 |
| IRAS 06035−7102 | <6.1 | 0.417 ± 0.004 | 0.233 ± 0.058 | 0.34 ± 0.10 | <11.6 | 0.023 |
| IRAS 06206−6315 | <2.9 | 0.129 ± 0.010 | 0.050 ± 0.005 | 0.059 ± 0.019 | <1.8 | 0.008 |
| IRAS 06301−7934 | <9.6[b] | 0.107 ± 0.020[b] | 0.044 ± 0.016[b] | 0.072 ± 0.017[b] | 0.095 ± 0.018 | 0.022 |
| IRAS 06361−6217 | <14.0[b] | 0.094 ± 0.004[b] | <2.1[b] | <0.3[b] | <2.3 | 0.011 |
| IRAS 07598+6508 | <3.0 | 0.138 ± 0.070 | 0.037 ± 0.006 | 0.067 ± 0.002 | <22.5 | 0.011 |
| IRAS 08311−2459 | <7.5 | 0.388 ± 0.030 | 0.252 ± 0.026 | 0.32 ± 0.10 | <2.6 | 0.019 |
| IRAS 08572+3915 | <15.4 | 0.119 ± 0.004 | 0.051 ± 0.010 | 0.046 ± 0.013 | <43.0 | 0.003 |
| IRAS 09022−3615[c] | <3.3 | 0.122 ± 0.008 | <0.2 | <0.2 | <0.04 | 0.001 |
| IRAS 09463+8141 | <4.4[b] | 0.108 ± 0.055[b] | 0.045 ± 0.022[b] | 0.083 ± 0.007[b] | <0.4 | 0.019 |
| IRAS 10091+4704 | <4.5[b] | <0.4[b] | <0.4[b] | <0.1[b] | <0.3 | ... |
| IRAS 10398+3247 | ... | <0.1[b] | <0.001[b] | <0.004[b] | <0.2 | ... |
| IRAS 10565+2448 | <10.9 | 0.657 ± 0.005 | 0.256 ± 0.009 | 0.403 ± 0.002 | <5.4 | 0.013 |
| IRAS 11119+3257 | <2.5 | <1.7 | <1.6 | 0.054 ± 0.007 | <9.1 | 0.003 |
| IRAS 12018+1941 | <2.6 | 0.093 ± 0.006 | 0.030 ± 0.003 | 0.043 ± 0.008 | <1.1 | 0.010 |
| IRAS 12032+1707 | <10.7[b] | 0.094 ± 0.030[b] | <1.5[b] | 0.077 ± 0.027[b] | 0.147 ± 0.044 | 0.028 |
| IRAS 12072−0444 | <4.5 | 0.192 ± 0.017 | 0.089 ± 0.010 | 0.136 ± 0.008 | <2.7 | 0.020 |
| IRAS 12112+0305 | 0.14 ± 0.04 | 0.412 ± 0.044 | 0.173 ± 0.031 | 0.237 ± 0.003 | 0.41 ± 0.08 | 0.021 |
| IRAS 12514+1027 | <0.7 | <0.5 | <0.5 | <0.2 | <4.0 | ... |
| IRAS 13120−5453 | <30.9 | 1.047 ± 0.034 | 0.662 ± 0.045 | 0.763 ± 0.005 | <14.6 | 0.008 |
| IRAS 13218+0552 | <1.8 | <1.5 | <8.9[b] | <9.4[b] | <16.9 | ... |
| IRAS 13342+3932 | 0.03 ± 0.01 | 0.102 ± 0.002 | <3.9[b] | <4.2[b] | <2.6 | 0.016 |
| IRAS 13352+6402 | <5.2[b] | <1.1[b] | <0.9[b] | 0.016 ± 0.008[b] | <1.2 | 0.002 |
| IRAS 13451+1232 | <4.5 | 0.283 ± 0.065 | 0.129 ± 0.005 | 0.219 ± 0.026 | <4.1 | 0.031 |
| IRAS 14348−1447 | <6.1 | 0.447 ± 0.015 | 0.195 ± 0.010 | 0.240 ± 0.021 | <3.1 | 0.017 |
| IRAS 14378−3651 | <6.6 | 0.193 ± 0.016 | 0.079 ± 0.016 | 0.125 ± 0.180 | <2.3 | 0.008 |
| IRAS 14537+1950 | ... | <0.1 | <0.2[b] | <0.1[b] | <0.1 | ... |
| IRAS 14548+3349 | ... | <0.2[b] | <0.2[b] | <0.1[b] | <0.2 | ... |
| IRAS 15001+1433 | <1.9 | 0.077 ± 0.007 | <2.8[b] | 0.068 ± 0.013[b] | <1.7 | 0.010 |
| IRAS 15206+3342 | <2.5 | 0.102 ± 0.053[b] | <4.3[b] | <2.6[b] | <1.6 | 0.006 |
| IRAS 15250+3609 | <12.9 | 0.156 ± 0.014 | 0.050 ± 0.006 | 0.048 ± 0.004 | <10.4 | 0.004 |
| IRAS 15462−0450 | <4.1 | 0.134 ± 0.006 | 0.037 ± 0.001 | 0.086 ± 0.012 | <5.7 | 0.010 |
| IRAS 16124+3241 | ... | <0.3[b] | <0.1[b] | <0.1[b] | <0.1 | ... |
| IRAS 16334+4630 | <4.2[b] | <0.9[b] | <0.7[b] | <0.4[b] | <0.4 | ... |
| IRAS 17068+4027 | <10.2[b] | 0.072 ± 0.018[b] | <1.7[b] | 0.052 ± 0.017[b] | 0.087 ± 0.019 | 0.020 |
| IRAS 17179+5444 | <1.7 | 0.209 ± 0.007 | 0.068 ± 0.024 | 0.14 ± 0.02 | <1.4 | 0.031 |
| IRAS 17208−0014 | <23.9 | 0.881 ± 0.009 | 0.497 ± 0.085 | 0.57 ± 0.11 | <8.5 | 0.009 |
| IRAS 17233+3712 | ... | <0.1 | <0.5[b] | <0.3[b] | <0.1 | ... |
| IRAS 17463+5806 | <3.5[b] | <0.6[b] | <0.3[b] | 0.023 ± 0.011[b] | <0.2 | 0.007 |
| IRAS 18030+0705 | <1.4[b] | 0.111 ± 0.008[b] | <0.8[b] | <0.4[b] | <0.2 | 0.008 |
| IRAS 18443+7433 | <15.5[b] | <2.7[b] | <2.4[b] | 0.048 ± 0.007[b] | <1.7 | 0.003 |
| IRAS 19254−7245 | <8.5 | 0.881 ± 0.057 | 0.382 ± 0.095 | 0.382 ± 0.004 | <0.4 | 0.031 |
| IRAS 19297−0406 | <4.8 | 0.332 ± 0.082[b] | <3.3[b] | 0.196 ± 0.008[b] | <1.7 | 0.009 |
| IRAS 19458+0944 | <19.3[b] | 0.219 ± 0.042[b] | <2.2[b] | 0.113 ± 0.038[b] | <1.0 | 0.009 |
| IRAS 20037−1547 | <11.2[b] | <5.8[b] | <4.4[b] | 0.081 ± 0.005[b] | <4.8 | 0.006 |
| IRAS 20087−0308 | <2.1 | 0.229 ± 0.014[b] | 0.084 ± 0.033[b] | 0.13 ± 0.04[b] | <2.2 | 0.011 |
| IRAS 20100−4156 | <4.6 | 0.083 ± 0.007 | 0.032 ± 0.001 | 0.068 ± 0.010 | <2.9 | 0.005 |
| IRAS 20414−1651 | <2.4 | 0.156 ± 0.003[b] | <1.6[b] | 0.049 ± 0.033[b] | <0.7 | 0.006 |
| IRAS 20551−4250 | <16.3 | 0.896 ± 0.052[b] | <18.0[b] | 0.443 ± 0.020[b] | <9.8 | 0.013 |
| IRAS 21272+2514 | <6.6[b] | <1.0[b] | <0.7[b] | 0.037 ± 0.002[b] | <0.5 | 0.004 |

TABLE 3—*Continued*

| Object | $S(0)$ 28.22 $\mu$m ($10^{-20}$ W cm$^{-2}$) | $S(1)$ 17.04 $\mu$m ($10^{-20}$ W cm$^{-2}$) | $S(2)$ 12.28 $\mu$m ($10^{-20}$ W cm$^{-2}$) | $S(3)$ 9.67 $\mu$m ($10^{-20}$ W cm$^{-2}$) | $S(7)$ 5.51 $\mu$m ($10^{-20}$ W cm$^{-2}$) | $L_{H_2}/L_{IR}$[a] (%) |
|---|---|---|---|---|---|---|
| IRAS 22491−1808 | <7.0 | 0.165 ± 0.005[b] | <3.1[b] | 0.098 ± 0.013[b] | <1.0 | 0.006 |
| IRAS 23128−5919 | <12.2 | 0.514 ± 0.010[b] | <22.595[b] | 0.305 ± 0.080[b] | <7.3 | 0.009 |
| IRAS 23129+2548 | <10.1[b] | <1.3[b] | <1.1[b] | <0.1[b] | <0.6 | ... |
| IRAS 23365+3604 | <9.1 | 0.390 ± 0.031 | 0.201 ± 0.095 | 0.31 ± 0.05 | <3.0 | 0.015 |
| IRAS 23498+2423 | <0.68 | <0.5 | <0.3 | <0.2 | <2.1 | ... |
| IRAS 23529−2119 | ... | <1.4[b] | <1.0[b] | 0.028 ± 0.011[b] | <0.7 | 0.010 |
| Mrk 231[d] | <67.5 | <31.7 | <26.8 | 0.46 ± 0.13 | <122.3 | 0.001 |
| Mrk 273 | <26.25 | 1.024 ± 0.009 | 0.56 ± 0.07 | 1.04 ± 0.09 | <15.0 | 0.015 |
| Mrk 463E | <7.9 | 0.279 ± 0.037 | 0.131 ± 0.008 | 0.28 ± 0.06 | <38.5 | 0.017 |
| Mrk 1014 | <4.2 | <2.5 | <1.5 | 0.07 ± 0.03 | <4.6 | 0.003 |
| NGC 6240 | 0.50 ± 0.25 | 4.271 ± 0.344 | 3.55 ± 0.26 | 5.83 ± 0.43 | 5.54 ± 0.50 | 0.097 |
| UGC 5101 | <10.0 | 0.496 ± 0.047 | 0.27 ± 0.05 | 0.28 ± 0.03 | <19.5 | 0.010 |

[a] Ratio of the sum of the $H_2$ line fluxes divided by the IR luminosity. The far-infrared luminosities are defined in Table 2.
[b] Emission lines observed using IRS-LORES.
[c] The absolute flux calibration for IRAS 09022−3615 is uncertain; see text.
[d] Both the $S(1)$ and $S(2)$ lines are present. However, we quote upper limits, as both lines are poorly calibrated. The $S(1)$ line straddles orders 12 and 11 in IRS-SH, and the center of $S(2)$ line profile is affected by bad pixel values.

also arise in PDRs associated with massive star formation. Higher angular resolution observations are needed to measure the relative fractions emitted from a dusty torus and from PDRs.

Using the same 27 sources we can test our assumption that the ortho-to-para ratio is 3. In Figure 7, the dashed line shows the theoretical $H_2$ $S(1)/S(2)$ line ratio as a function of $T_{ex}$, and we have overplotted the observed line ratios. The data are consistent with the assumed ortho-para ratio of 3 with essentially no extinction. In both Figures 6 and 7, the ULIRG IRAS 15462−0450 shows the largest departure from the theoretical curves, which we attribute to calibration difficulties.

### 3.3. *Multitemperature* $H_2$ *Gas*

ULIRGs are complex systems, and we would not expect the $H_2$ gas to be at a single temperature. NGC 6240 (Armus et al. 2006a) is the only system in our sample where we detect all the $S(0)$–$S(7)$ rotational lines. Its excitation diagram is shown in Figure 8. The $S(3)$–$S(7)$ lines are well fit by a hot $H_2$ component, with $T_{ex} = 1327 \pm 36$ K. The $S(7)$ line flux implies a hot molecular hydrogen mass of $(4.1 \pm 0.8) \times 10^6$ $M_\odot$. Subtracting this component's contribution from the $S(0)$–$S(3)$ lines gives a second, cooler $H_2$ component, with $T_{ex} = 292 \pm 6$ K. The measured $S(0)$ line flux weights the fit to lower temperatures and correspondingly larger $H_2$ masses. The warm gas mass inferred for the $S(0)$ line flux is $(6 \pm 3) \times 10^8$ $M_\odot$.

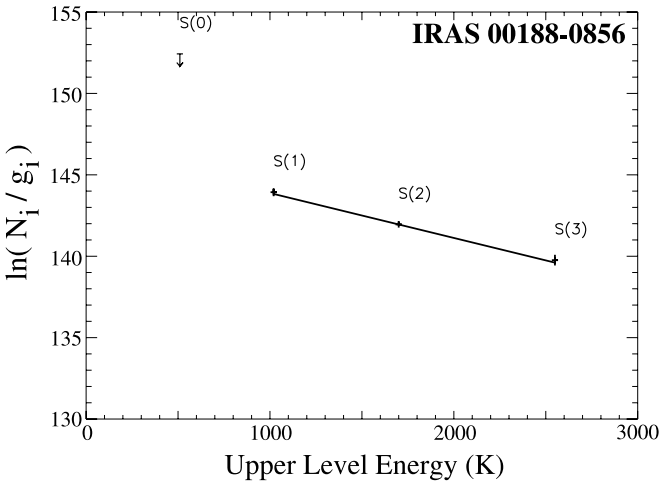


FIG. 4.—Molecular hydrogen excitation diagram for IRAS 00188−0856, which is typical for our ULIRG sample. The solid line shows a fit to the $S(1)$, $S(2)$, and $S(3)$ measurements, which is consistent with a single temperature component at $T_{ex} = 358 \pm 25$ K, with a mass of $4.1 \times 10^7$ $M_\odot$. The arrow shows the 3 $\sigma$ upper limit for the $S(0)$ transition.

Besides NGC 6240, we detect the $S(0)$ line in only two other sources, IRAS 12112+0305 and IRAS 13342+3932. Likewise, the $S(7)$ line is detected in only six sources, NGC 6240 Arp 220, IRAS 06301−7934, IRAS 12032+1707, IRAS 12112+0305, and IRAS 17068+4027 with S/N > 3. Figure 9 shows the excitation diagrams for these six sources. When the $S(7)$ line is detected, a fit is first made to the $S(7)$ and $S(3)$ lines to determine the temperature of the hot $H_2$ component. In Arp 220, for example, the derived excitation temperature is $1435 \pm 120$ K. This component's contribution is then subtracted from the $S(3)$–$S(0)$ lines, so the $T_{ex}$ and mass of the cooler $H_2$ component can be estimated. The derived $T_{ex}$ and $H_2$ masses are listed in Table 4. In IRAS 13342+3932 the fit is heavily weighted toward a low temperature, as only the $S(0)$ and $S(1)$ lines are detected. The resulting gas mass is an order of magnitude larger than the masses calculated for NGC 6240 and IRAS 12112+0305. A similar decrease of ~50–100 K in the temperature and increase in the mass by a factor of 10 are obtained for both NGC 6240 and IRAS 12112+0305 if only the $S(0)$ and $S(1)$ lines are used in the second temperature fit. This suggests that our result for both the mass and temperature in IRAS 13342+3932 is strongly biased by our nondetection of the $S(2)$ and $S(3)$ lines. Using the average temperature for the sample ($T_{ex} = 336 \pm 15$ K), we infer a mass of $\sim 2 \times 10^8$ $M_\odot$, which is probably a better estimate of the warm $H_2$ gas mass, and more in keeping with the rest of the sample. The average hot gas temperature is $1400 \pm 60$ K, with an associated molecular mass of $(3 \pm 2) \times 10^6$ $M_\odot$. The warm, $T_{ex} \sim 340$ K $H_2$ component, with $M_{H_2} \sim 10^8$–$10^9$ $M_\odot$, thus represents the bulk of the measured gas mass.

## 4. DISCUSSION

### 4.1. *Warm and Cold ULIRGs*

Figure 10 shows the derived $H_2$ mass as a function of the IRAS 25 and 60 $\mu$m flux density ratio ($F_{25\,\mu m}/F_{60\,\mu m}$). The vertical dashed line corresponds to $F_{25\,\mu m}/F_{60\,\mu m} = 0.2$, which is used to

TABLE 4

PROPERTIES OF THE WARM MOLECULAR $H_2$

| Object (1) | $T_{ex}$ (K) (2) | Warm $M_{H_2}$ ($10^7\ M_\odot$) (3) | Cold $M_{H_2}$ ($10^{10}\ M_\odot$) (4) | Warm $M_{H_2}$/Cold $M_{H_2}$ (%) (5) |
|---|---|---|---|---|
| Arp 220 | 1435 ± 20 | 0.03 ± 0.02 | ... | ... |
| | 258 ± 4 | 6.6 ± 0.8 | ... | ... |
| | | | 3.72[a] | 0.18 |
| IRAS 00188−0856 | 358 ± 25 | 4.11 ± 1.18 | 3.98[a] | 0.10 |
| IRAS 00397−1312 | 365 ± 24 | 13.16 ± 3.69 | ... | ... |
| IRAS 00406−3127[L] | ⟨336 ± 15⟩ | 32.04 ± 11.95 | ... | ... |
| IRAS 01003−2238 | 365 ± 19 | 6.68 ± 2.71 | ... | ... |
| IRAS 02115+0226[L] | ⟨336 ± 15⟩ | 69.14 ± 26.08 | ... | ... |
| IRAS 03521+0028 | 317 ± 11 | 14.67 ± 3.14 | 5.62[a] | 0.26 |
| IRAS 04114−5117[L] | 321 ± 26 | 11.74 ± 4.05 | ... | ... |
| IRAS 05189−2524 | 380 ± 30 | 2.86 ± 1.82 | 0.26[b] | 1.1 |
| IRAS 06035−7102 | 363 ± 23 | 13.94 ± 3.30 | 4.17[c] | 0.33 |
| IRAS 06206−6315 | 313 ± 15 | 8.14 ± 1.76 | 9.33[c] | 0.09 |
| IRAS 06301−7934[L] | 1329 ± 106 | 0.3 ± 0.1 | ... | ... |
| | 264 ± 14 | 32 ± 10 | ... | ... |
| IRAS 06361−6217[L] | ⟨336 ± 15⟩ | 16.56 ± 2.93 | ... | ... |
| IRAS 07598+6508 | 366 ± 22 | 17.53 ± 9.65 | 6.76[a] | 0.26 |
| IRAS 08311−2459 | 384 ± 22 | 19.27 ± 4.23 | ... | ... |
| IRAS 08572+3915 | 310 ± 18 | 2.93 ± 0.76 | 0.72[c] | 0.41 |
| IRAS 09022−3615 | ⟨336 ± 15⟩ | 2.61 ± 0.48 | ... | ... |
| IRAS 09463+8141[L] | 363 ± 39 | 15.10 ± 9.80 | ... | ... |
| IRAS 10565+2448 | 338 ± 1 | 7.05 ± 0.10 | 3.02[c] | 0.23 |
| IRAS 11119+3257 | ⟨336 ± 15⟩ | 23.21 ± 9.14 | ... | ... |
| IRAS 12018+1941 | 309 ± 11 | 22.26 ± 3.63 | ... | ... |
| IRAS 12032+1707[L] | 1471 ± 196 | 0.5 ± 0.5 | ... | ... |
| | 309 ± 30 | 38 ± 20 | ... | ... |
| IRAS 12072−0444 | 349 ± 8 | 19.32 ± 2.39 | ... | ... |
| IRAS 12112+0305 | 1428 ± 1049 | 0.2 ± 0.8 | ... | ... |
| | 271 ± 5 | 119 ± 41 | ... | ... |
| | | | 0.49[d] | 24 |
| IRAS 13120−5453 | 348 ± 3 | 5.29 ± 0.24 | ... | ... |
| IRAS 13342+3932 | 141 ± 15 | 803 ± 459 [S(0)] | ... | ... |
| | ⟨336 ± 15⟩ | 23.15 ± 0.46 | ... | ... |
| IRAS 13352+6402[L] | ⟨336 ± 15⟩ | 11.10 ± 7.04 | ... | ... |
| IRAS 13451+1232 | 366 ± 18 | 23.30 ± 6.85 | 0.51[d] | 4.57 |
| IRAS 14348−1447 | 328 ± 6 | 19.86 ± 1.61 | 3.47[d] | 0.57 |
| IRAS 14378−3651 | 320 ± 31 | 5.97 ± 2.42 | 2.29[c] | 0.26 |
| IRAS 15001+1433[L] | 346 ± 40 | 17.05 ± 11.10 | ... | ... |
| IRAS 15206+3342[L] | ⟨336 ± 15⟩ | 10.45 ± 5.72 | ... | ... |
| IRAS 15250+3609 | 294 ± 7 | 3.89 ± 0.53 | ... | ... |
| IRAS 15462−0450 | 285 ± 5 | 12.57 ± 1.15 | ... | ... |
| IRAS 17068+4027[L] | 1416 ± 154 | 0.2 ± 0.2 | ... | ... |
| | 292 ± 23 | 22 ± 9 | ... | ... |
| IRAS 17179+5444 | 340 ± 13 | 30.03 ± 4.61 | ... | ... |
| IRAS 17208−0014 | 347 ± 13 | 8.93 ± 1.29 | 3.80[a] | 0.23 |
| IRAS 17463+5806[L] | ⟨336 ± 15⟩ | 29.87 ± 17.70 | ... | ... |
| IRAS 18030+0705[L] | ⟨336 ± 15⟩ | 16.01 ± 3.00 | ... | ... |
| IRAS 18443+7433[L] | ⟨336 ± 15⟩ | 9.71 ± 3.87 | ... | ... |
| IRAS 19254−7245 | 313 ± 4 | 23.63 ± 1.99 | 4.57[c] | 0.52 |
| IRAS 19297−0406[L] | 334 ± 18 | 15.39 ± 5.02 | 5.25[a] | 0.29 |
| IRAS 19458+0944[L] | 325 ± 27 | 14.94 ± 5.80 | 6.76[a] | 0.22 |
| IRAS 20037−1547[L] | ⟨336 ± 15⟩ | 35.92 ± 13.50 | ... | ... |
| IRAS 20087−0308[L] | 326 ± 21 | 17.49 ± 4.69 | 9.33[a] | 0.1875 |
| IRAS 20100−4156 | 339 ± 12 | 9.05 ± 1.46 | ... | ... |
| IRAS 20414−1651[L] | 294 ± 38 | 10.04 ± 5.70 | ... | ... |
| IRAS 20551−4250[L] | 322 ± 5 | 10.46 ± 0.90 | 2.82[c] | 0.37 |
| IRAS 21272+2514[L] | ⟨336 ± 15⟩ | 9.49 ± 3.55 | ... | ... |
| IRAS 22491−1808[L] | 335 ± 10 | 6.09 ± 0.74 | 4.27[c] | 0.14 |
| IRAS 23128−5919[L] | 335 ± 19 | 6.04 ± 1.36 | 1.95[c] | 0.31 |
| IRAS 23365+3604 | 358 ± 14 | 8.62 ± 1.45 | 4.68[a] | 0.18 |
| IRAS 23529−2119[L] | ⟨336 ± 15⟩ | 81.05 ± 43.67 | ... | ... |
| Mrk 231 | ⟨336 ± 15⟩ | 7.97 ± 3.73 | 4.07[a] | 0.20 |

TABLE 4—*Continued*

| Object (1) | $T_{ex}$ (K) (2) | Warm $M_{H_2}$ ($10^7$ $M_\odot$) (3) | Cold $M_{H_2}$ ($10^{10}$ $M_\odot$) (4) | Warm $M_{H_2}$/Cold $M_{H_2}$ (%) (5) |
|---|---|---|---|---|
| Mrk 273 | 378 ± 8 | 6.75 ± 0.52 | 2.69[a] | 0.25 |
| Mrk 463E | 368 ± 21 | 3.50 ± 0.87 | 0.04[d] | 8.75 |
| Mrk 1014 | ⟨336 ± 15⟩ | 20.38 ± 12.20 | 5.25[a] | 0.39 |
| NGC 6240 | 1327 ± 36 | 0.41 ± 0.08 | ... | ... |
| | 292 ± 6 | 62 ± 32 | ... | ... |
| | | | 4.37[a] | 1.43 |
| UGC 5101 | 332 ± 11 | 4.75 ± 0.78 | 0.62[b] | 0.77 |

NOTES.—The warm molecular $H_2$ mass is derived from our data. HIRES observations are used when available, and the LORES observations are marked in the first column with an "L." The temperature is derived from the fit to the $S(1)$–$S(3)$ data. The mass is derived using the $S(1)$ line flux; if this line is not detected, the $S(3)$ line flux is used. If only a single line is detected, we use the average temperature of 336 ± 15 K to estimate the mass, denoted by angle brackets in col. (2). The standard Milky Way $H_2$ mass-to-CO luminosity ratio, $\alpha = 4.6\,M_\odot\,(\mathrm{K\ km\ s^{-1}\ pc^2})^{-1}$, has been used to estimate the cold gas mass. However, Solomon et al. (1997) argue that $\alpha \sim 1.4$ should be used for ULIRGs. This would decrease the cold gas mass and correspondingly increase the warm gas fraction by a factor of ~3. The $S(7)$ line is detected in Arp 220, IRAS 06301−7934, IRAS 12032+1707, IRAS 12112+0305, IRAS 17068+4027, and NGC 6240, and we calculate a hot gas mass. The $S(0)$ line is detected in IRAS 12112+0305, IRAS 13342+3932, and NGC 6240, which lowers the warm gas temperature. The $S(0)$ line flux is used to estimate the gas mass. For IRAS 13342+3932 we only detect the $S(0)$ and $S(1)$ lines, resulting in a much lower gas temperature. We also quote the gas mass using the average temperature for the sample, which may be a more reasonable estimate of the gas mass. There is a problem with the absolute flux calibration for IRAS 09022−3615, and the mass could be a factor of 20 higher than quoted.

[a] Solomon et al. (1997).
[b] Rigopoulou et al. (1996).
[c] Mirabel et al. (1990).
[d] Evans et al. (2002).

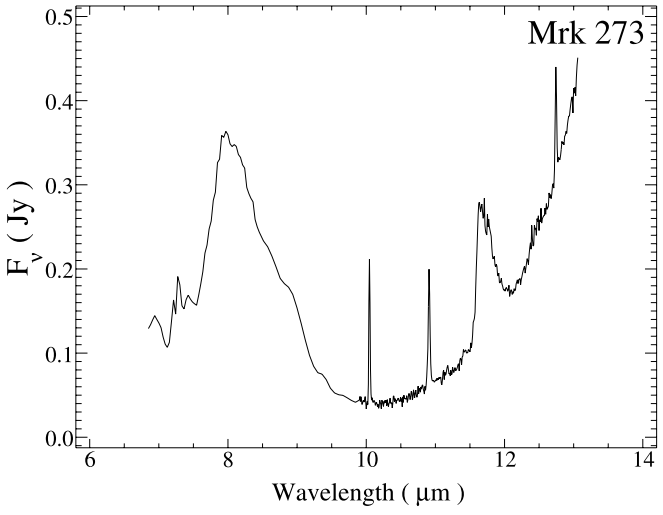


FIG. 5.—Combined IRS-LORES (6.5–9.8 $\mu$m) and IRS-HIRES (9.8–13.1 $\mu$m) spectrum for Mrk 273. The $x$-axis is the observed wavelength. A deep 9.7 $\mu$m silicate absorption trough is apparent, indicating heavy extinction ($A_V \sim$ 20–40) toward the active nucleus. On the other hand, the ratio of the $S(3)$ 9.67 $\mu$m to $S(2)$ 12.28 $\mu$m $H_2$ lines implies much lower levels of extinction, implying that little of the absorbing material lies in a screen between the warm $H_2$ and us.

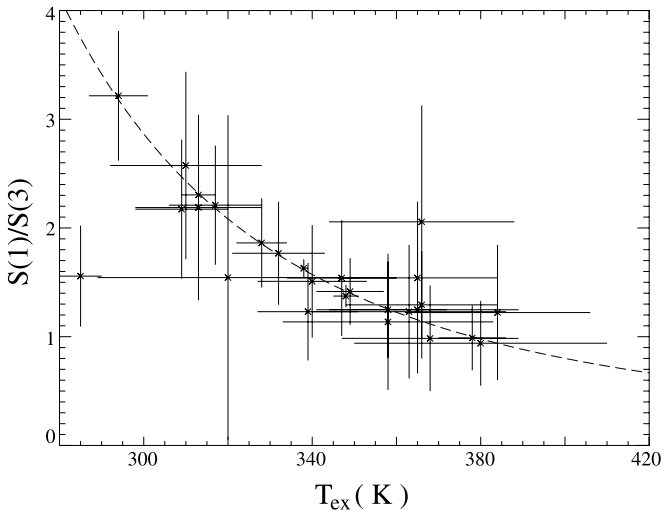


FIG. 6.—Molecular hydrogen $S(1)/S(3)$ line ratios as a function of the derived temperature ($T_{ex}$) for 27 ULIRGs (excluding Arp 220 and IRAS 12112+0305) with at least three $J \leq 4$ HIRES line measurements. The intrinsic (unreddened) ratio is shown as a dashed line. Extinction toward the warm $H_2$ component is minimal in most of the sources.

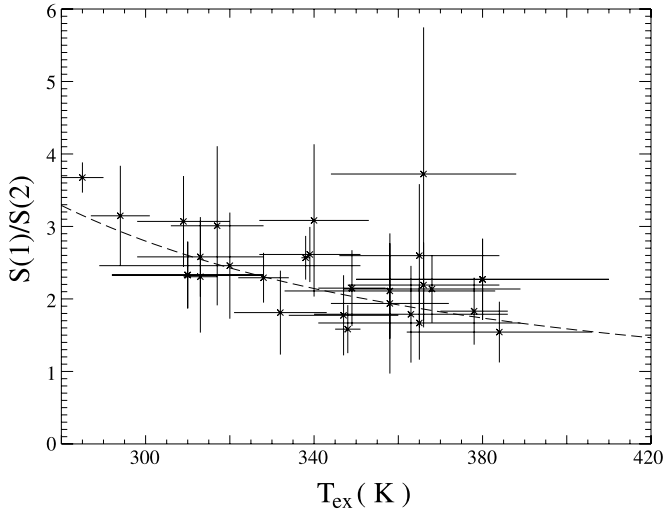


FIG. 7.—Molecular hydrogen $S(1)/S(2)$ line ratios as a function of the derived excitation temperature ($T_{ex}$) for the 27 ULIRGs in Fig. 8. The dashed line shows the expected trend for an ortho-to-para ratio of 3 and no extinction, which is consistent with the data.

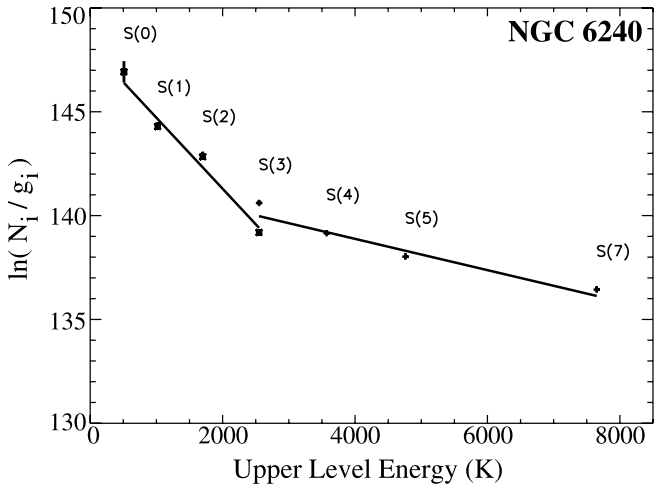


FIG. 8.—Molecular hydrogen excitation diagram for NGC 6240. The $S(3)$–$S(7)$ values can be fit by a hot ($T_{ex} = 1327 \pm 36$ K) $H_2$ component. A second cooler ($T_{ex} = 292 \pm 6$ K) gas component is found after subtracting this component from the $S(0)$–$S(3)$ values (*replotted as asterisks*) prior to modeling.

separate cold and warm ULIRGs. There are no obvious trends. That is, there appears to be no systematic tendency for starburst- or AGN-powered ULIRGs to have systematically larger (or smaller) masses of warm $H_2$.

Likewise, there is no clear dependence on far-infrared luminosity. Figure 11 shows the derived warm $H_2$ mass as a function of the 60 $\mu$m specific luminosity ($L_{60\,\mu m}$), which we define as $4\pi d_L^2 F_{60\,\mu m}$ in units of W Hz$^{-1}$. Here $d_L$ is the source's luminosity distance. The 27 ULIRGs in the plot all have $z < 0.1$, which ensures that the IRAS 60 $\mu$m flux densities correspond to nearly identical rest-frame wavelengths. A possible tendency for warm $H_2$ mass to increase with far-infrared luminosities in excess of $L_{60\,\mu m} = 3 \times 10^{25}$ W Hz$^{-1}$ is significantly weakened by a number of outliers with higher $H_2$ masses.

The observed $S(1)$ line intensity is typically $\sim 10^{-4}$ ergs cm$^{-2}$ s$^{-1}$, which is consistent with the Burton et al. (1992) PDR models with density $\sim 10^4$–$10^5$ cm$^{-3}$ and far-UV fields of $\sim 10^3 G_0$–$10^4 G_0$. Here $G_0$ is the local interstellar far-UV radiation field, determined to be $1.6 \times 10^{-3}$ ergs s$^{-1}$ cm$^{-2}$ (Habing 1968). This is consistent with PDRs being a large contributor to the warm $H_2$ emission. Of course, there can also be a significant shock component in some ULIRGs. Constraining the contribution of shock excitation will require observations of rovibrational transitions in the near-infrared.

### 4.2. *Fractional Warm Gas Mass*

In Table 4 we have listed the cold molecular hydrogen mass derived from $^{12}$CO (1–0) observations of 30 ULIRGs from the literature. These masses range from $10^8$ to $10^{11}$ $M_\odot$, with an average cold $M_{H_2} \sim 4 \times 10^{10}$ $M_\odot$. This is calculated using the standard Milky Way $M_{H_2}/L_{CO}$ ratio of 4.6 $M_\odot$ (K km s$^{-1}$ pc$^2$)$^{-1}$ determined from observations of Galactic molecular clouds (Solomon et al. 1987). However, as stressed by Maloney & Black (1988), because the CO (1–0) line intensity scales as a modest power of the gas temperature,[9] the molecular hydrogen masses may be *overestimated* by factors of 3–5 in regions of intense star formation or AGN dominance. The density and filling factor of the $^{12}$CO (1–0) emitting regions also affect the measured CO intensity in ways that are difficult to take into account a priori. Solomon et al. (1997) argue that the standard conversion factor is inappropriate for ULIRGs, as the derived masses often exceed the dynamical masses. They argue that in the extreme environments found in the central regions of ULIRGs, the CO emission originates not from self-gravitating clouds but from an intercloud medium, which is bound by the potential of the galaxy or molecular gas pressure, resulting in a smaller $M_{H_2}/L_{CO}$ of $\sim 1.4$ $M_\odot$ (K km s$^{-1}$ pc$^2$)$^{-1}$. All of this suggests that the cold molecular masses in Table 4 should be viewed with considerable caution and likely represent overestimates of the true $M_{H_2}$. Indeed, use of the $\alpha$ advocated by Solomon et al. (1997) for their ULIRG sample would both lower the cold $H_2$ mass and increase the warm $H_2$ gas fraction by a factor of $\sim 3$. However, the warm $H_2$ gas remains a small fraction of the total $H_2$ mass.

We have $H_2$ detections for 28 of these sources. Some of the sources do have a warm gas fraction that scales with warm gas mass, but the scatter in the data is large and there is no strong trend. The median fractional warm gas mass is 0.3% of the cold gas mass. Figure 12 shows the warm gas fraction as a function of $F_{25\,\mu m}/F_{60\,\mu m}$. Rigopoulou et al. (2002) derived an average gas temperature of $\sim 150$ K for their sample of local starbursts and AGNs and found the warm gas fraction to be as large as 10% in starbursts and up to 35% (with a large scatter) in Seyfert galaxies. In nearly half of their sample they did not detect the $S(0)$ line, and the derived temperature is $\sim 300$ K. The difference between the average warm gas fractions in our ULIRG sample and the local starburst/AGN sample is heavily weighted by the adopted gas temperature and whether or not the $S(0)$ line is detected. It is likely that the warm gas fraction is similar in both. More sensitive observations of the $S(0)$ line in ULIRGs are needed to fully constrain the $\sim 150$ K component.

Figure 12 also shows that only eight of 28 ULIRGs with both cold and warm $H_2$ masses have $F_{25\,\mu m}/F_{60\,\mu m} > 0.2$, and only one has $F_{25\,\mu m}/F_{60\,\mu m} \geq 0.4$. As a result, we are unable to say conclusively whether there is a tendency for the warm $H_2$ mass to depend on dust temperature, i.e., on AGN dominance. While the position of Mrk 463 in the upper right of the figure is suggestive of such a trend, it may simply be an outlier, like the cold IRAS 12112+0305 near the upper left. No increase in the warm gas

[9] $I_{CO} \propto T_{kin}^{1.3}$ for $T_{kin} \lesssim 30$ K, and $I_{CO} \propto T_{kin}$ for $T_{kin} > 30$ K.

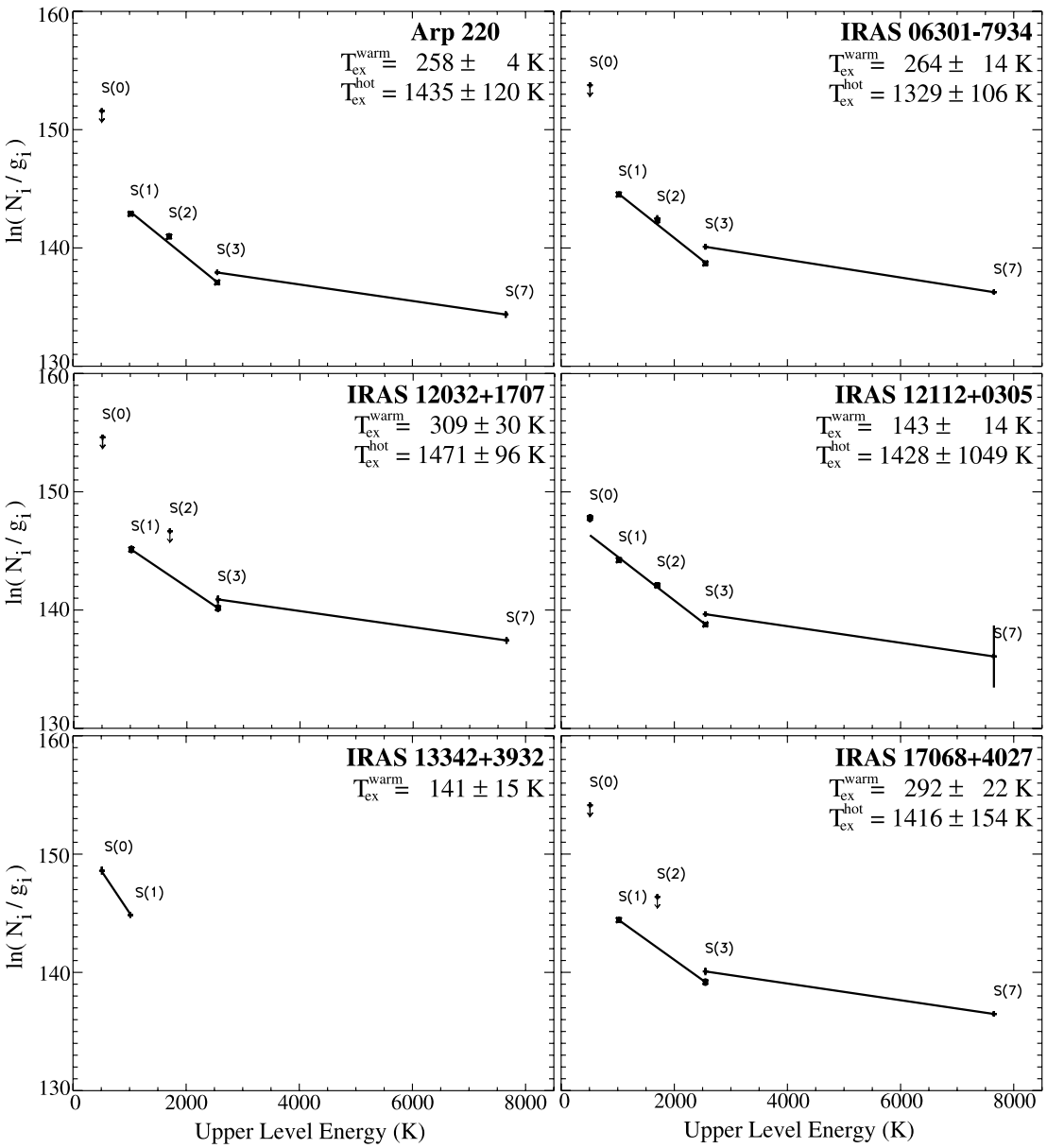


FIG. 9.— Excitation diagrams for the six ULIRGs with $S(0)$ and/or $S(7)$ line detections. In five sources, the $S(7)$ and $S(3)$ values are fit by a single hot $H_2$ component, which is subtracted from the $S(0)$–$S(3)$ values (or limits) to characterize molecular hydrogen gas at a cooler temperature. The derived warm ($T_{ex}^{warm}$) and hot ($T_{ex}^{hot}$) excitation temperatures are given in the upper right of each panel.

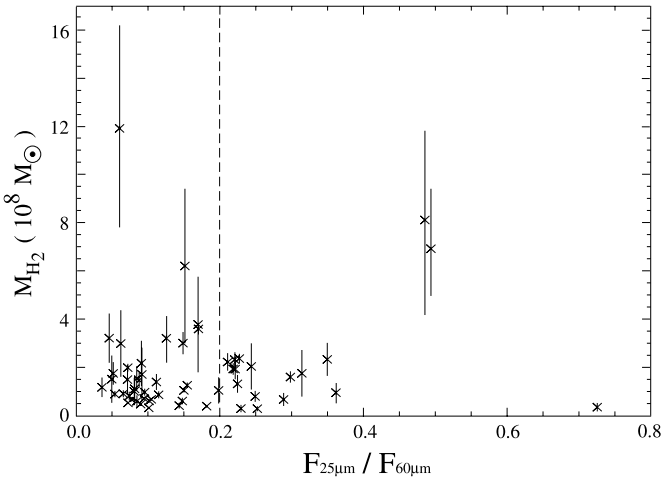


FIG. 10.—Derived warm $H_2$ masses for the ULIRG sample as a function of their IRAS 25 to 60 $\mu$m flux density ratios. The vertical line ($F_{25\,\mu m}/F_{60\,\mu m} = 0.2$) is thought to separate sources dominated by starbursts ($F_{25\,\mu m}/F_{60\,\mu m} < 0.2$) from those powered primarily by an enshrouded active nucleus ($F_{25\,\mu m}/F_{60\,\mu m} > 0.2$). No obvious relation between warm $H_2$ mass and $F_{25\,\mu m}/F_{60\,\mu m}$ is present.

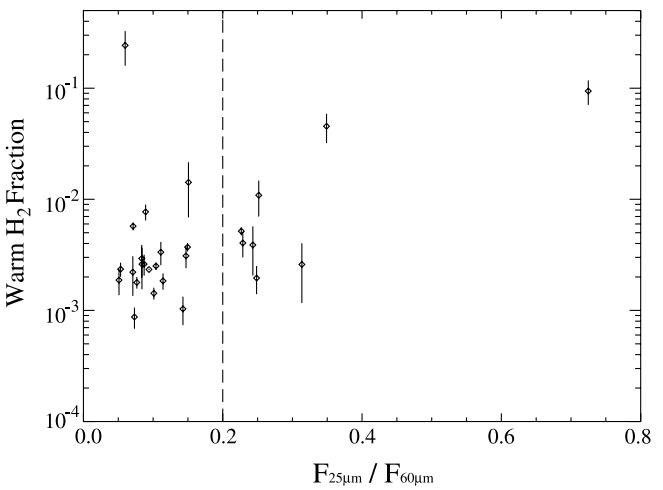


FIG. 12.—Ratio of the warm $H_2$ mass to the cold $H_2$ mass from $^{12}$CO observations as a fraction of the *IRAS* 25 to 60 $\mu$m flux density ratio. The dashed line separates cool and warm ULIRGs, i.e., those that appear to be powered primarily by obscured starbursts or active nuclei, respectively.

fraction is measured as a function of either increasing *IRAS* 25 or 60 $\mu$m specific luminosity.

## 5. CONCLUSIONS

We have used *Spitzer*'s IRS to obtain spectra from 5.0 to 38.5 $\mu$m for a large sample of ULIRGs. This sample is bright (0.1 Jy $< F_{60\,\mu m} \leq$ 104 Jy) and hase redshifts between 0.02 and 0.93. We have detected line emission from pure rotational transitions of molecular hydrogen in 77% of the sample and in all ULIRGs with $F_{60\,\mu m} > 2$ Jy. The majority of these sources are modeled with a single-temperature $H_2$ component, with an average excitation temperature ($T_{ex}$) of 336 $\pm$ 15 K. The ULIRGs contain large quantities of warm molecular hydrogen. We find an average mass of $2 \times 10^8$ $M_\odot$. Large optical depths, as inferred from the depth of the silicate absorption trough at 9.7 $\mu$m, are not observed along the line of sight to the warm $H_2$ gas. If the gas originates in a central dusty torus, the medium must be clumpy.

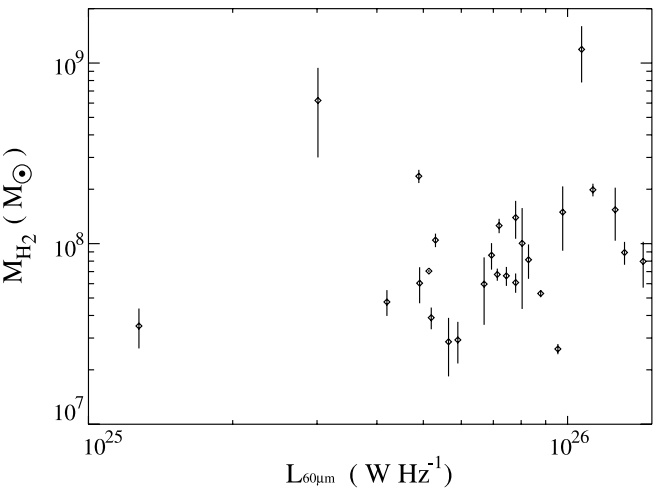


FIG. 11.—Warm $H_2$ masses as a function of the *IRAS* derived 60 $\mu$m specific luminosity ($L_{60\,\mu m}$, in W $Hz^{-1}$) for the 27 ULIRGs with $z < 0.1$. There is no clear tendency for more 60 $\mu$m luminous ULIRGs to possess larger $M_{H_2}$.

The warm $H_2$ mass does not appear to depend on the *IRAS* 25 to 60 $\mu$m flux density ratio, which is used to classify ULIRGs into "warm" (AGN dominated) and "cold" (starburst dominated) categories. Similarly, the warm $H_2$ mass does not scale with the specific luminosity at 25 or 60 $\mu$m. A possible common origin for the gas is from photodissociation regions associated with massive star formation.

The single-temperature gas model, fitted to the $S(1)$–$S(3)$ lines, is a simplification, and the gas is likely to have multiple temperature components. Detection of the $S(0)$ line will typically lower the derived temperature in the single component fit by 50–100 K, leading to a larger estimated gas mass. This higher gas mass cannot be ruled out in the bulk of our sample for which we do not detect the $S(0)$ line. A hot $H_2$ gas component is inferred when the $S(7)$ line is detected. This line is detected in six ULIRGs and is modeled as a $T_{ex} = 1400 \pm 60$ K $H_2$ component, with a relatively small mass ($M_{H_2} \sim 3 \times 10^6$ $M_\odot$).

Using cold molecular gas estimates from $^{12}$CO observations in the literature, we find that the warm $H_2$ mass is typically less than 1% of the cold $H_2$ mass. The average warm gas fraction could be a few tens of percent, but this requires verification through the detection of the $S(0)$ 28.22 $\mu$m line, which is difficult using the IRS, as the line is situated in a low-sensitivity region of the detector array, and detection of the $^{12}$CO line. In general, ULIRGs have a warm mass fraction that is comparable to that found in local starburst and Seyfert galaxies (Rigopoulou et al. 2002).

This work is based (in part) on observations made with the *Spitzer Space Telescope*, which is operated by the Jet Propulsion Laboratory, California Institute of Technology, under NASA contract 1407. Support for this work was provided by NASA through contract 1257184 issued by JPL/Caltech.

We wish to thank Paul Goldsmith, David Hollenbach, Alberto Noriego-Crespo, and Terry Herter for useful discussions concerning the excitation of molecular hydrogen, Bill Reach for the zodiacal light model, and James Houck for making the IRS possible.

REFERENCES

Adams, T. F., & Weedman, D. W. 1972, ApJ, 173, L109
Arakelian, M. A., Dibai, E. A., Esipov, V. F., & Markarian, B. E. 1971, Astrofiz., 7, 177
Armus, L., et al. 2004, ApJS, 154, 178
———. 2006a, ApJ, 640, 204
———. 2006b, ApJ, submitted
Burton, M. G., Hollenbach, D. J., & Tielens, A. G. 1992, ApJ, 399, 563
Cohen, M., Megeath, T. G., Hammersley, P. L., Martin-Luis, F., & Stauffer, J. 2003, AJ, 125, 2645
Cutri, R., et al. 2003, 2MASS All-Sky Catalog of Point Sources (Pasadena: IPAC/Caltech), http://irsa.ipac.caltech.edu/applications/Gator
Elbaz, D., & Cesarsky, C. J. 2003, Science, 300, 270
Evans, A. S., Mazzarella, J. M., Surace, J. A., & Sanders, D. B. 2002, ApJ, 580, 749
Evans, A. S., Surace, J. A., & Mazzarella, J. M. 2000, ApJ, 529, L85
Habart, E., Walmsley, C. M., Verstraete, L., Cazaux, S., Maiolino, R., Cox, P., Boulanger, F., & Pineau des Forêts, G. 2005, Space Sci. Rev., 119, 71
Habing, H. J. 1968, Bull. Astron. Inst. Netherlands, 19, 421
Higdon, S. J. U., et al. 2004, PASP, 116, 975
Houck, J. R., et al. 2004, ApJS, 154, 18
Kim, D.-C., & Sanders, D. B. 1998, ApJS, 119, 41
Kormendy, J., & Sanders, D. B. 1992, ApJ, 390, L53
Lonsdale, C. J., Lonsdale, C. J., Smith, H. E., & Diamond, P. J. 2003, ApJ, 592, 804
Lutz, D., Sturm, E., Genzel, R., Spoon, H. W. W., Moorwood, A. F. M., Netzer, H., & Sternberg, A. 2003, A&A, 409, 867
Maloney, P., & Black, J. H. 1988, ApJ, 325, 389
Mirabel, I. F., Booth, R. S., Garay, G., Johansson, L. E. B., & Sanders, D. B. 1990, A&A, 236, 327
Moorwood, A. F. M. 1996, Space Sci. Rev., 77, 303
Neugebauer, G., et al. 1984, ApJ, 278, L1
Reach, W. T., Morris, P., Boulanger, F., & Okumura, K. 2003, Icarus, 164, 384
Rigopoulou, D., Kunze, D., Lutz, D., Genzel, R., & Moorwood, A. F. M. 2002, A&A, 389, 374
Rigopoulou, D., Lawrence, A., White, G. J., Rowan-Robinson, M., & Church, S. E. 1996, A&A, 305, 747
Roche, P. F., & Aitken, D. K. 1985, MNRAS, 215, 425
Sanders, D. B., & Mirabel, I. F. 1996, ARA&A, 34, 749
Sanders, D. B., Scoville, N. Z., & Soifer, B. T. 1991, ApJ, 370, 158
Sanders, D. B., Soifer, B. T., Elias, J. H., Madore, B. F., Matthews, K., Neugebauer, G., & Scoville, N. Z. 1988, ApJ, 325, 74
Soifer, B. T., Sanders, D. B., Madore, B. F., Neugebauer, G., Danielson, G. E., Elias, J. H., Lonsdale, C. J., & Rice, W. L. 1987, ApJ, 320, 238
Solomon, P. M., Downes, D., Radford, S. J. E., & Barrett, J. W. 1997, ApJ, 478, 144
Solomon, P. M., Rivolo, A. R., Barrett, J. W., & Yahil, A. 1987, ApJ, 319, 730
Stanford, S. A., Stern, D., van Breugel, W., & De Breuck, C. 2000, ApJS, 131, 185
Strauss, M. A., Huchra, J. P., Davis, M., Yahil, A., Fisher, K B., & Tonry, J. 1992, ApJS, 83, 29
Sturm, E., et al. 1996, A&A, 315, L133
Valentijn, E. A., van der Werf, P. P., de Graauw, T., & de Jong, T. 1996, A&A, 315, L145
van der Werf, P. P., Genzel, R., Krabbe, A., Blietz, M., Lutz, D., Drapatz, S., Ward, M. J., & Forbes, D. A. 1993, ApJ, 405, 522
Werner, M. W., et al. 2004, ApJS, 154, 1